ACS NANO

www.acsnano.org

Nanoscale Resolution Imaging of Whole Mouse Embryos Using Expansion Microscopy

Jueun Sim,○○○ Chan E. Park,○○○ In Cho,○○○ Kyeongbae Min, Minho Eom, Seungjae Han, Hyungju Jeon, Eun-Seo Cho, Yunjeong Lee, Young Hyun Yun, Sungho Lee, Deok-Hyeon Cheon, Jihyun Kim, Museong Kim, Hyun-Ju Cho, Ji-Won Park, Ajeet Kumar, Yosep Chong, Jeong Seuk Kang, Kiryl D. Piatkevich, Erica E. Jung, Du-Seock Kang, Seok-Kyu Kwon, Jinhyun Kim, Ki-Jun Yoon, Jeong-Soo Lee, Cheol-Hee Kim, Myunghwan Choi, Jin Woo Kim, Mi-Ryoung Song, Hyung Jin Choi, Edward S. Boyden, Young-Gyu Yoon,* and Jae-Byum Chang*

Cite This: *ACS Nano* 2025, 19, 7910−7927

Read Online

ACCESS | Metrics & More | Article Recommendations | Supporting Information

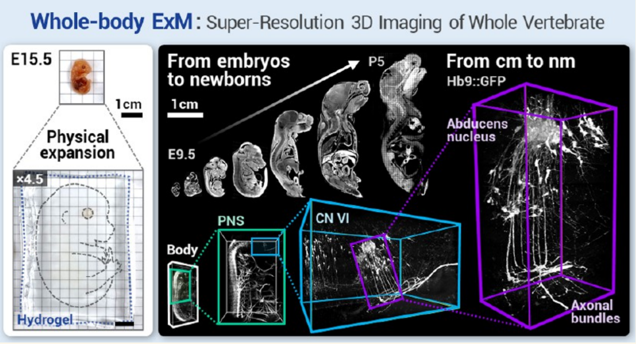

ABSTRACT: **Nanoscale imaging of whole vertebrates is essential for the systematic understanding of human diseases, yet this goal has not yet been achieved. Expansion microscopy (ExM) is an attractive option for accomplishing this aim; however, the expansion of even mouse embryos at mid- and late-developmental stages, which have fewer calcified body parts than adult mice, is yet to be demonstrated due to the challenges of expanding calcified tissues. Here, we introduce a state-of-the-art ExM technique, termed whole-body ExM, that utilizes cyclic digestion. This technique allows for the super-resolution, volumetric imaging of anatomical structures, proteins, and endogenous fluorescent proteins (FPs) within embryonic and neonatal mice by expanding them 4-fold. The key feature of whole-body ExM is the alternating application of two enzyme compositions repeated multiple times. Through the simple repetition of this digestion process with an increasing number of cycles, mouse embryos of various stages up to E18.5, and even neonatal mice, which display a dramatic difference in the content of calcified tissues compared to embryos, are expanded without further laborious optimization. Furthermore, the whole-body ExM's ability to retain FP signals allows the visualization of various neuronal structures in transgenic mice. Whole-body ExM could facilitate studies of molecular changes in various vertebrates.**

KEYWORDS: *expansion microscopy, super-resolution imaging, whole-body imaging, embryo imaging, peripheral nerve system*

INTRODUCTION

A systematic understanding of biological systems requires an unbiased investigation into entire vertebrate bodies, not just specific organs, at subcellular resolutions.[1−3] For instance, in developmental biology, a high spatial resolution is essential to discern changes in subcellular structures during different developmental stages, whereas full spatial coverage is needed for organ morphogenesis analysis from a systematic perspective.[4] This type of high-resolution panoptic imaging is also crucial for researching nervous systems, as changes in cellular organelles or nanoscale neuronal structures must be observed across the entire body.[5,6] Various imaging techniques, including tissue clearing,[5−12] computed tomography,[13] and electron microscopy,[14] have been developed to visualize the whole organism. Computed tomography and tissue clearing do not rely on physical sectioning, allowing for noninvasive, three-dimensional histological analysis.[2,13] These techniques have a resolution of 0.5−2 μm, which is sufficient for imaging micron-scale morphological and molecular structures.[13] Using these techniques, neural projections from the brain to internal organs have been imaged throughout the vertebrate body.[5,6,9] Electron microscopy, on the other hand, can achieve a resolution of up to 3 nm on ultrathin specimens.[15] Electron microscopy has been combined with automated sectioning and successfully

Received: October 19, 2024
Revised: December 18, 2024
Accepted: December 23, 2024
Published: February 18, 2025

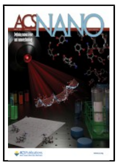

https://doi.org/10.1021/acsnano.4c14791

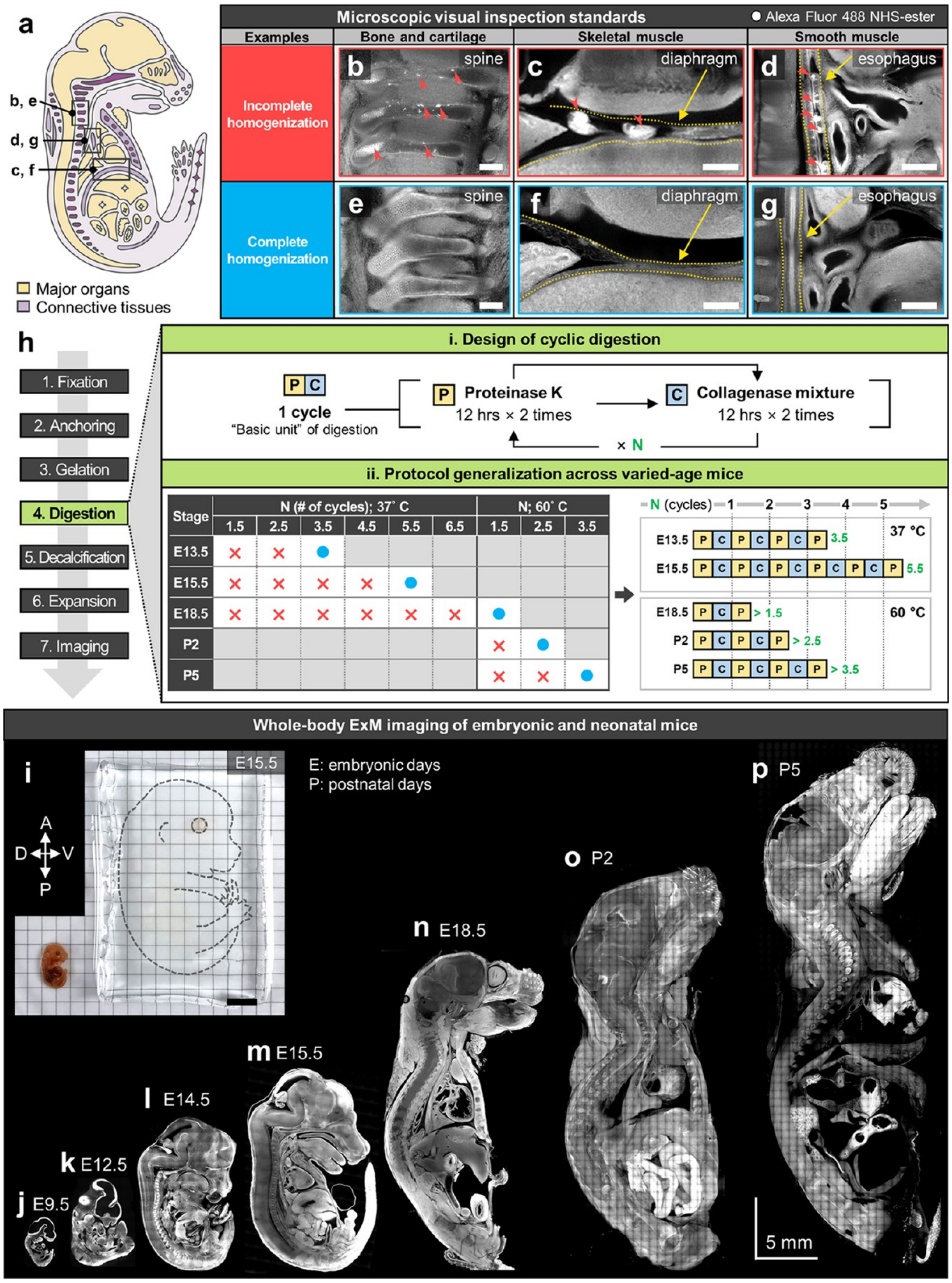

Stage	N (# of cycles); 37° C						N; 60° C		
	1.5	2.5	3.5	4.5	5.5	6.5	1.5	2.5	3.5
E13.5	×	×	●						
E15.5	×	×	×	×	●				
E18.5	×	×	×	×	×	×	●		
P2							×	●	
P5							×	×	●

Figure 1. Development and generalization of the whole-body ExM protocol. (a−g) Examples of visually inspecting the complete homogenization of specimens at the microscopic level. The images in the table are representative confocal images of 500-μm-thick E15.5 mouse embryo slices stained with fluorophore NHS ester and expanded in deionized water. (a) Schematic illustration summarizing anatomical features in an E15.5 mouse embryo, including major organs (yellow) and connective tissues (purple). (b−d) Microscopic deformations observed in the specimens post expansion due to incomplete homogenization during the digestion process: (b−d) each represent the spine, diaphragm, and esophagus, respectively; red arrowheads, deformation resulting from local distortion of the specimen. (e−g) Completely homogenized and uniformly expanded mouse embryo slices after sufficient digestion: (e−g) each represent the spine, diaphragm, and esophagus, respectively. (h) Overview of whole-body ExM workflows and the concept of cyclic digestion: i. design of cyclic digestion; ii. protocol generalization across mice of varying ages. (i) A representative photograph of E15.5 whole mouse embryos before and after the whole-body ExM process: left side of the photo, an unexpanded half-embryo; right side, its 4.5-fold expanded counterpart. (j−p) Representative confocal images of expanded mice from early embryonic to neonatal stages: (j) an E9.5 whole mouse embryo; (k) an E12.5 whole mouse embryo; (l) a half E14.5 mouse embryo; (m) a 500-μm-thick E15.5 mouse embryo slice; (n) a 500-μm-thick E18.5 mouse embryo slice; (o) a 1 mm-thick P2 mouse slice; (p) a 500-μm-thick P5 mouse slice. Staining: (b−g), (j, k), (m, n), and p, Alexa Fluor 488 NHS ester; (l) ATTO 647N NHS ester; (o) CF568 NHS ester. Scale bars: (b, e) 200 μm; (c, f) 500 μm; (d, g) 200 μm; (i) 1 cm; and (j−p) 5 mm. All length scales are presented in pre-expansion dimensions.

imaged the nanoscale details of neuronal structures, even individual synaptic vesicles, over a hundred microns.[15,16] However, what is missing is a technique that enables the imaging of centimeter-sized entire vertebrate bodies with the sub-100 nm resolution required to resolve the nanoscale details of cellular organelles and dense neural structures.

Expansion microscopy (ExM) is an attractive candidate for satisfying such needs. It can image biomolecules with a lateral resolution of 60 nm by physically expanding the specimens.[17,18] The ExM procedure also optically clears specimens, enabling the acquisition of images from specimens with a thickness of hundreds of microns without the need for thin-sectioning.[17] ExM has been successfully used on a variety of specimens, including cultured cells,[17,19−31] animal organ slices,[17,23−36] entire mouse organs,[36] *Drosophila* brains,[37,38] and zebrafish larvae brains.[39] ExM has also been used on entire organisms, including parasite microorganisms,[37,40] *Caenorhabditis elegans*,[41] larval zebrafish, and early-stage mouse embryos.[42] Despite these successes, adapting ExM for the super-resolution imaging of entire vertebrate bodies, particularly mice, presents two significant challenges. First, no protocol has yet been developed for expanding mouse bodies containing mineralized tissues, such as bones and cartilage. The size and composition of the mouse body vary substantially, depending on the developmental stage. For example, mouse embryos at E10.5, where organogenesis is just beginning, measure about 5 mm in length and weigh approximately 0.03 g. In contrast, newborn mice at post natal day 5 reach an average body length of about 41 mm—more than eight times longer—and a weight of 3.5 g—over a hundred times heavier (Figure S1).[43,44] More importantly, significant bone mineralization, which poses the key challenge in expanding mouse embryos, occurs between the ages of E14.5 and E16. This period marks the transition from cartilaginous precursors to the deposition of a mineralized bone matrix (see Supporting Note 1 for a detailed discussion).[45−48] As such, mouse embryos exhibit a considerable variation in body composition across developmental stages. The primary gap identified is the absence of an ExM protocol that is both easily applicable and adaptable for mice over such a wide range of developmental stages, encompassing a broad spectrum of hard tissue content, including that of newborn mice.

To overcome these challenges, we introduce a state-of-the-art ExM technique, termed whole-body ExM, which enables a more than 4-fold expansion of bodies from all mouse embryonic stages and neonatal mice, facilitating super-resolution imaging of these specimens. The key to whole-body ExM is the development of an advanced digestion process of hydrogel-embedded specimens prior to expansion. We first demonstrate that employing a cyclic digestion process in which proteinase K and a collagenase mixture are alternately applied and repeated allows for the uniform expansion of mouse embryos, including those with bones and cartilage. Then, to broaden the technique's applicability, we show that simply increasing the total number of digestion cycles (n) is sufficient to expand even neonatal specimens. We demonstrate that whole-body ExM preserves the fluorescence signals of genetically expressed fluorescent proteins (FPs), antibody staining, and panmolecular staining of anatomical structures. Using this method, we achieve super-resolution three-dimensional (3D) imaging of diverse neuronal structures across the entire bodies of various transgenic mouse lines.

RESULTS AND DISCUSSION

Development of Whole-Body ExM. We first applied a well-established ExM protocol based on proteinase K digestion to the expansion of mouse embryos. In this experiment, 500 μm-thick sagittal slices of mouse embryos at E15.5 were chosen as representative models of vertebrates with calcified bone and cartilage. Briefly, fixed embryo slices were first treated with 6-((acryloyl)amino)hexanoic acid (AcX) to make all proteins in the specimens gel-anchorable and then embedded in a swellable hydrogel. After gelation, specimens were digested with proteinase K, as the conventional ExM protocol.[23] During the digestion, we stained samples with fluorophore NHS esters to label all proteins in the sample.[19,27,30,49] In the fluorophore NHS-ester staining, we confirmed that protein structures labeled with fluorophore NHS esters depended on the hydrophobicity of the fluorophores. Hydrophilic fluorophores, such as Alexa Fluor 488, labeled the nucleoplasm and showed uniform staining in the cytoplasm. Hydrophobic fluorophores, such as ATTO 647N, labeled lipid-rich structures, such as nuclear membranes, Golgi apparatus, and mitochondria (see Supporting Notes 2−4 and Figures S2−S6 for a detailed discussion). In the expansion of mouse embryos, the hydrophilic fluorophore NHS ester was used to outline the morphology of anatomical structures, allowing a close visual inspection of sample distortion under the microscope. Even after a 144 h digestion with proteinase K, however, some tissues were not fully digested, leading to tissue distortion being observed post expansion (Figure S7a). We noted that such tissue distortion predominantly occurred at the interfaces between different types of tissues or organs, primarily in areas of connective tissues rather than occurring randomly within each organ (Figure 1a summarizes the major organs and connective tissues in the mouse embryo).

In applications of ExM in tissue slices or single types of organs excised from the body, these connective tissues would not need to be considered or would need to be considered to a lesser extent—but they become critical when expanding large, mechanically heterogeneous specimens, such as a vertebral body. Among various connective tissues, we found that fully homogenizing special connective tissues, such as bone and cartilage, and dense connective tissues, such as muscles and tendons, presented the greatest challenge. For instance, in the vertebral column, incomplete homogenization was obvious in the marginal regions between each vertebra and surrounding tissues, resulting in less expansion and thus brighter fluorescence signals (Figures 1b and S7b). Similarly, the lumen of the esophagus, composed of thick layers of smooth muscle,[50] and the diaphragm, made of multiple layers of skeletal muscles and tendons,[51] also showed incomplete homogenization (Figures 1c,d and S7c,d). Under a confocal microscope, such visual clues of incomplete homogenization become more apparent when compared with the same regions in samples that had been completely homogenized through optimized digestion (described below), as shown in Figure 1e−g.

Given that most connective tissues predominantly consist of collagen fibers,[52−55] we employed a mixture of collagenases to ensure the efficient homogenization of these components. The replacement of half the duration of digestion (i.e., 72 h) with collagenase mixture treatment greatly reduced such tissue damage, as shown in Figure S7f−j. Although collagenase is known to be relatively mild and therefore less effective than

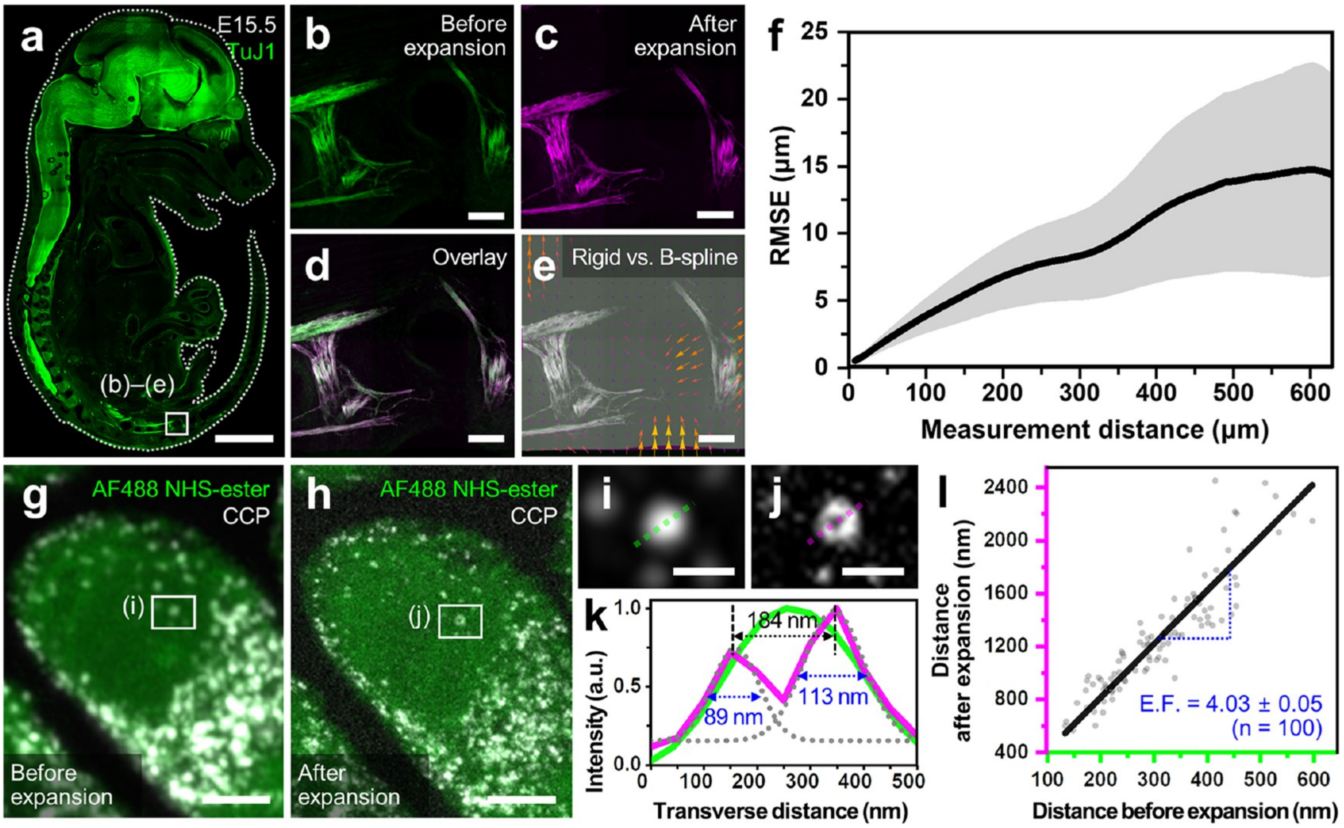

Figure 2. Validation of whole-body ExM isotropy at micro- and nanoscales. (a−f) Microscopic isotropy analysis. (a) A representative confocal image of a 500-μm-thick E15.5 mouse embryo slice stained with antibody against TuJ1 (green). (b, c) Magnified images of boxed regions in a: (b) before expansion and (c), after expansion. (d) Overlay image of b and rigidly registered c with scaled rotation. (e) Deformation vector field map computed by comparing rigidly registered and nonrigidly registered (via b-spline) images. (f) RMSE as a function of measurement length before and after whole-body ExM processing: black line, mean; shaded area, standard deviation; RMSE, 3.20 ± 0.77% on average at a measurement distance of 0−620 μm (calculated from 11 different ROIs from three samples). (g−l) Nanoscopic isotropy analysis. (g, h) Representative confocal image of a 500-μm-thick E15.5 mouse embryo slice stained with Alexa Fluor 488 NHS ester (AF 488 NHS ester; green) and antibody against CCP (gray): (g) before expansion and (h), after expansion. (i, j) Magnified views of the boxed regions in g, h, respectively. (k) Intensity profiles along the path indicated in i, j: green line, before expansion; magenta line, after expansion; gray dotted line, Gaussian-fitted line profile along the magenta line; full-width at half-maximum of individual peaks, 89 and 113 nm; peak-to-peak distance, 184 nm. (l) Scatterplot of distance measured after expansion versus before expansion: black line, linear fit; measured expansion factor (=slope of the fitted line), 4.03 ± 0.05 (n = 100 from three different samples). Radii of single CCPs and distances between the nearby CCPs were measured. Scale bars: (a) 2 mm; (b−e) 100 μm; (g, h) 2 μm; (i, j) 500 nm. All length scales are presented in pre-expansion dimensions.

proteinase K in homogenizing hydrogel-embedded tissue samples,[41] we found that using collagenase along with proteinase K is more effective than using only proteinase K for the same duration.

We then focused on designing an optimal digestion protocol to ensure the complete homogenization of the mouse embryos. It was necessary to consider the sequence and duration of the treatment of the samples with two different enzymes. For the purpose of simplification, we devised a "cyclic digestion process", in which the sample is repeatedly treated with proteinase K and collagenase mixtures alternately at regular intervals. We defined one "cycle" of the digestion process as a total of 48 h of treatment, namely, two 12 h treatments with proteinase K followed by two 12 h treatments with a collagenase mixture, and designed the whole digestion process as n-times the simple repetition of this cycle (schematic diagram (i) in Figure 1h). As depicted in Figure S8, the cyclic digestion process is the best option due to the simplicity of the experimental design as well as the potential scalability of the protocol for mice of varied ages.

We then validated whether the whole-body ExM protocol could be applied to embryos aged up to E18.5 and even at the neonatal stage. In this range, both the size of specimens and, more importantly, the mechanical properties of the samples vary dramatically, as discussed in the introduction.[46−53] We hypothesized that by solely varying the total digestion cycles, n, while controlling all other experimental variables, we could achieve a 4-fold expansion of samples at various developmental stages and thereby generalize the whole-body ExM protocol. To prove this, we screened an optimized number of digestion cycles for mouse embryos at different stages. Mouse embryos at E13.5, E15.5, and E18.5 stages were sectioned into 500 μm thicknesses and underwent whole-body ExM processing with progressively increasing digestion cycles. During this process, variables other than the total digestion cycles and volume of the buffer were kept constant. To ensure complete digestion, microscopic visual inspections were carried out on all samples, with successful expansion determined by the absence of tissue distortion in any region. Figure S9 presents representative confocal images that highlight regions of frequent tissue

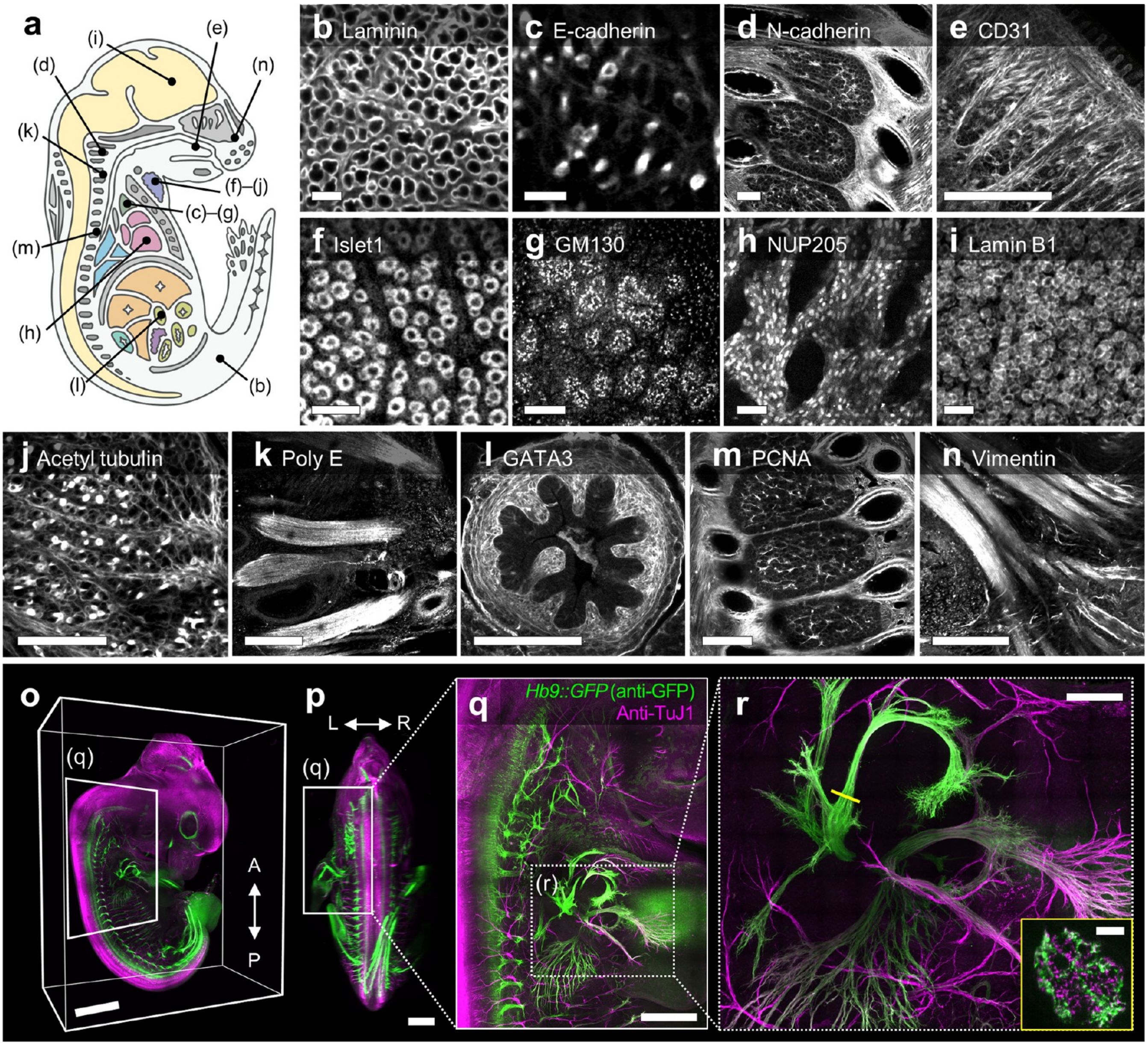

Figure 3. Validation of whole-body ExM compatibility with immunolabeling. (a) A schematic diagram shows an E15.5 mouse embryo, indicating the locations referenced in b−n. (b−n) Representative confocal images of expanded 500-μm-thick E15.5 mouse embryo slices immunolabeled with a different antibody as follows: (b), anti-laminin; (c), anti-E-cadherin; (d), anti-N-cadherin; (e), anti-CD31; (f), anti-islet1; (g), anti-GM130; (h), anti-NUP205; (i), anti-lamin B1; (j), anti-acetyl tubulin; (k), anti-poly E; (l), anti-GATA3; (m), anti-PCNA; and (n), anti-vimentin. (o−p) Confocal image of a 2-fold expanded *Hb9::GFP* transgenic whole mouse embryo at E12.5, whole mount immunostained for TuJ1 (magenta) and Hb9::GFP (green). (q) Magnified image of the boxed region in o, p, but after 4.5-fold expansion. (r) Magnified view of the boxed region in q, imaged with a 25×/0.95 NA objective. Bottom right panel: a cross-sectional view of the radial motor axon (yellow line). Expansion factors: (b−p) 2-fold and (q−r) 4.5-fold. Scale bars: (b, c) 20 μm; (d, e) 100 μm; (f−i) 20 μm; (j) 50 μm; (k−n) 200 μm; (o−q) 1 mm; (r) 100 μm; and inset of (r) 10 μm. All length scales are presented in pre-expansion dimensions.

distortion due to incomplete homogenization alongside those depicting complete homogenization in the same areas. For example, severe tissue distortion was observed in all three samples in the group of E15.5 embryo slices treated for 2.5 cycles. Mild but still noticeable tissue distortion was found in the groups treated for 3.5 and 4.5 cycles. In contrast, after 5.5 cycles of treatment, all samples were completely homogenized, and no signs of insufficient digestion were observed post expansion (Figure S10). Therefore, we concluded that 5.5 digestion cycles are suitable for the uniform 4-fold expansion of E15.5 embryo slices. In this approach, we were able to determine the total digestion cycles required for the uniform 4-fold expansion of embryo slices at different developmental stages. Hydrogel-embedded mouse embryos expanded 4-fold through whole-body ExM and became almost completely transparent, except for the eyes (Figure 1i). In embryos more developed than E15.5, such as those at E18.5, cyclic digestion treatments exceeding 13.5 cycles did not result in complete homogenization. However, by increasing the digestion temperature to 60 °C to enhance enzyme activity, we found that 1.5 cycles of digestion were sufficient to achieve complete homogenization of E18.5 mouse embryos. Conducting cyclic digestion at 60 °C enabled us to apply whole-body ExM even further to neonatal mouse slices at post natal days 2 and 5 (Figures 1j−p and S11).

Validation of Whole-Body ExM Isotropy. To validate whether whole-body ExM preserves microscopic architecture without significant deformation, we quantified the root-mean-square error (RMSE) of feature measurements after whole-body ExM. We immunostained E15.5 mouse embryo slices with a neuron-specific class III β-tubulin (TuJ1) antibody and acquired images both before and after the whole-body ExM process (Figure 2a−c). We selected a total of 11 distinct regions proximal to the bones where hard body parts and soft tissues are intertwined and expected to exhibit the highest degree of deformation during physical expansion. The RMSE for each region was computed from the registered before- and after-expansion images, as described previously (Figure 2d,e; see Validation of Isotropy in the Experimental Section for detailed information).[23,24] We observed an RMSE of ∼6.7% of the measured lengths over the range of 0−620 μm (Figure 2f; total of 11 regions of interest (ROIs) from three different samples). Considering that the RMSE values of published ExM protocols range from ∼2−4% for mouse brain slices to ∼1−6% for whole invertebrate organisms,[23,41] this indicates that whole-body ExM maintains a similar level of isotropy to that of reported ExM protocols, despite expanding much larger and more complex vertebrate samples.

For nanoscale validation, we immunostained clathrin-coated pits (CCP), a feature traditionally used to characterize the performance of super-resolution microscopes.[56] Specimens were imaged with an LSM980 confocal microscope in Airyscan2 mode before expansion and with a spinning disk confocal microscope after expansion (Figure 2g,h). Whole-body ExM resolved the central nulls of the pits well (Figure S12), even inside vertebrate bones (Figure 2i,j). After expansion, the thickness of the CCP presented full-width at half-maximum (fwhm) values of 89 and 113 nm, with a diameter of 184 nm (Figure 2k), closely matching the known value (100−200 nm).[57] We then measured the radii of single CCPs and the distance between two nearby CCPs and calculated the expansion factor. The expansion factor remained consistently at 4.03 ± 0.05 within the range of 130−600 nm (Figure 2l; confidence interval 0.009 with $P < 0.05$, $n = 100$ from three samples), indicating that whole-body ExM preserves nanoscale spatial organization.

Validation of Whole-Body ExM Compatibility with Molecular Labeling Methods. Next, we tested the compatibility of whole-body ExM with conventional molecular labeling techniques. First, we asked whether the signals of genetically encoded FPs inside of the specimens could be retained during the whole-body ExM process. We first tested this proposition with zebrafish (*Danio rerio*), a model vertebrate that is significantly smaller in size than a mouse at a similar developmental stage (average body length of 3.76 mm at 6 days post-fertilization [dpf]).[58] We expanded 6 dpf zebrafish larvae from three different transgenic lines, *flk1::eGFP*, *cmlc2::eGFP*, and *mbp::mGFP*, and then imaged FPs expressed throughout the body. Despite the difference in species, whole-body ExM protocols with 5.5 cycles were successfully applied to zebrafish, resulting in the 4-fold expansion of the whole larval body. More importantly, fluorescent signals of FPs were well preserved after a total of 264 h of prolonged digestion and expansion for all three transgenic lines investigated. For example, in *flk1::eGFP* larvae,[59] flk1 expression in vasculature was clearly visualized from head to tail (Figure S13a−c). Additionally, cmlc2, known to be expressed in cardiac tissue,[60] exhibited particularly strong expression in the ventricle and was well-mapped (Figure S13d,e). As shown in Figure S13f,g, the fluorescent signal of another tested reporter, mGFP, was also well preserved, allowing for the observation of myelination in neural tracts within a developing *mbp:mGFP* larval zebrafish, as in the previous study.[61]

In addition to FPs, we found that fluorescent signals inside the immunolabeled samples were well-preserved post whole-body ExM. To ensure compatibility, we labeled E15.5 mouse embryo slices with various antibodies against subcellular compartments, cytoskeletons, extracellular matrix components, neuronal markers, and disease markers and proceeded to the whole-body ExM process. As shown in Figure 3a−n, the antibody staining channel showed the characteristic expression patterns of each target protein in accordance with the literature.[62−66] The whole-body ExM's ability to retain fluorescent signals was particularly valuable when observing multiple proteins within a single vertebrate system was required. We immunostained the whole body of the *Hb9::GFP* mouse embryo[67] with anti-GFP and anti-TuJ1 antibodies and proceeded to the whole-body ExM process to generate a body-wide map of neuronal networks. In the expanded whole mouse embryo at E12.5, TuJ1 marked all neurons comprising the central and peripheral nerve systems, while Hb9 indicated somatic motor neurons exclusively (Figure 3o−p). As shown in Figure 3q,r, it was possible to specifically identify the Hb9$^+$ motor axon bundle among the TuJ1$^+$ brachial plexus by the high resolution offered by whole-body ExM. Overall, the whole-body ExM was compatible with standard molecular labeling methods and therefore holds potential for diverse applications in biological and medical research.

Although we have demonstrated that the antibody signals in samples were well retained with a high signal-to-noise ratio (SNR) during the whole-body ExM process, the decrease in signal intensity after expansion could pose a challenge to the observation of proteins expressed at particularly low levels. In this case, whole-body ExM can be combined with a signal amplification method that was developed for general ExM.[68] This method involved using anti-Alexa Fluor 488 antibodies that specifically bind to Alexa Fluor 488 fluorescent molecules. By repeated treatment of the samples with antibodies conjugated to Alexa Fluor 488 and anti-Alexa Fluor 488 antibodies, fluorescent signals could be amplified. To prove that such a simple signal amplification method can be applied to whole-body ExM, which employs an extended digestion duration, we first labeled the nine proteins, each exhibiting different expression levels, in the mouse brain slices. The slices were then embedded in hydrogels, digested, and subsequently subjected to signal amplification. (see Signal Amplification in the Experimental Section for the detailed process). As shown in Figure S14, we confirmed effective signal amplifications for all targets, with amplification ratios ranging from a minimum of 4.8-fold to a maximum of 10.9-fold ($n = 30$ for each of the nine samples).

Use of Whole-Body ExM in the Nanoscale Visualization of Developing Neuronal Systems. We then applied whole-body ExM to various transgenic mouse embryos to investigate body-wide neuronal distribution in developing embryos. The major neural distributions belonging to the

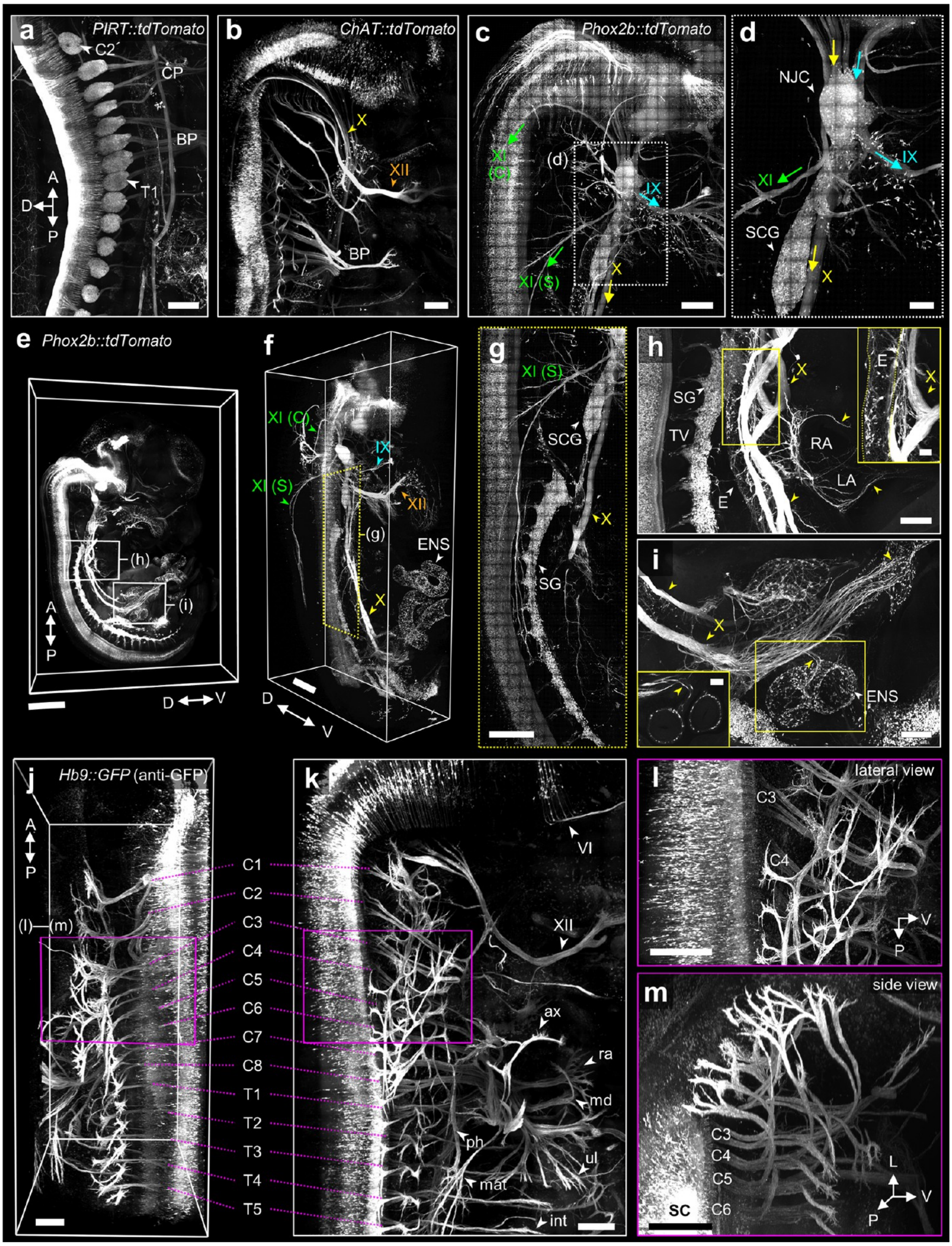

Figure 4. Mapping various neuronal systems of developing mouse embryos using whole-body ExM. (a) Confocal image of an expanded half-*PIRT::tdTomato* embryo at E16.5. CP, cervical plexus; BP, brachial plexus; C2, cervical dorsal root ganglion 2; T1, thoracic dorsal root ganglion 1. (b) Confocal image of an expanded half-*ChAT::tdTomato* embryo at E15.5. X, vagus nerve; XII, hypoglossal nerve; CP, cervical plexus; and BP, brachial plexus. (c) Confocal image of an expanded half-*Phox2b::tdTomato* embryo at E14.5. XI (C), cranial component of accessory nerve; XI (S), spinal component of accessory nerve; X, vagus nerve; IX, glossopharyngeal nerve. (d) Magnified view of the boxed region in c, showing Phox2b expression in the nodose-jugular complex (NJC) and superior cervical ganglion (SCG), and associated nerves. IX, glossopharyngeal nerve (cyan arrow); X, vagus nerve (yellow arrow); and XI, accessory nerve (green arrow). (e) Volumetric view of the half-*Phox2b::tdTomato* embryo. (f) High-magnification image showing phox2b$^+$ expression in the glossopharyngeal nerve (IX), vagus nerve (X), cranial component of the accessory nerve (XI (C)), spinal component of the accessory nerve (XI (S)), hypoglossal nerve (XII), and enteric nervous system (ENS). (g) Magnified view of the boxed region in f, showing lateral view of the accessory nerve (XI), superior cervical ganglion (SCG), vagus nerve (X), and sympathetic ganglions (SG). (h) Magnified views of the boxed regions in e, showing NJC-arising vagal sensory axons (yellow arrowheads) projecting toward the developing heart. Inset shows magnified views of the yellow boxed region, highlighting vagus nerve innervation to the esophagus. E, esophagus; RA, right atrium; LA, left atrium; SG, sympathetic ganglion; TV,

Figure 4. continued

thoracic vertebrae. (i) Magnified views of the boxed regions in e, showing NJC-arising vagal sensory axons (yellow arrowheads) projecting toward the developing gut, innervating to the enteric nervous system (ENS). Inset shows a single *z*-plane image of the yellow boxed region. (j−m) Confocal images of an expanded half-*Hb9::GFP* embryo at E13.5, stained with anti-GFP post digestion. (j) Dorsal view showing somatic motor neuron projections along the vertebral column. Cn, *n*-th cervical spinal nerves; Tn, *n*-th thoracic spinal nerves; (k) lateral view of j. VI, abducens nerve; XII, hypoglossal nerve; ax, axillary projection of forelimb nerves; ra, radial projection of forelimb nerves; md, median projection of forelimb nerves; ul, ulnar projection of forelimb nerves; mat, medial anterior thoracic projection of forelimb nerves; ph, phrenic nerves; int, intercostal nerves. (l, m) Magnified views of the boxed region in j, k, showing multiview of the somatic nerve projection. Images in b−g and j−k, were post-image processed for better visualization (see Imaging and Data Processing in the Experimental Section for detailed information). Direction: A, anterior; P, posterior; D, dorsal; V, ventral; and L, lateral. Scale bars: (a−c) 300 μm; (d) 100 μm; (e) 1 mm; (f, g) 500 μm; (h) 200 μm; insets of (h) 50 μm; (i) 200 μm; insets of (i) 200 μm; (j−m) 200 μm. All length scales are presented in pre-expansion dimensions.

peripheral nervous system (PNS) were successfully visualized in detail. Since the neuronal distribution in the body is symmetrical, transgenic mouse embryos were sliced along the midline into sagittal sections and subjected to the whole-body ExM process. In E16.5 half-PIRT::tdTomato embryos, strong PIRT protein expression was observed in the dorsal root ganglion (DRG) along the spinal cord, as is well-known.[69] Additionally, the projections of sensory neurons extending in different directions from each ganglion were mapped in three dimensions (Figure 4a). In contrast to PIRT, which was primarily distributed in the sensory neurons of the PNS,[70] ChAT was strongly expressed in the ventral root of the E15.5 embryo, where motor neuron projections originate, within a similar anatomical area. Apart from the spinal nerves, the projections of cranial nerves, including the facial nerve (VII), accessory nerve (XI), and hypoglossal nerve (XII), which originate in the brain and extend to the trunk region, were also evident (Figure 4b). In the *Phox2b::tdTomato* embryo at E14.5, the viscerosensory ganglia and associated nerves, essential components of the automatic nervous system (ANS), were mapped (Figure 4c). The nerve bundles extending from the hindbrain converged around the nodose-jugular complex (NJC) and then were projected to different parts of the body, as shown in Figure 4d. The improved spatial resolution and full spatial coverage provided by whole-body ExM enabled detailed investigation of three major tracks: the glossopharyngeal nerve (IX), extending from the most ventral side, passed through the NJC and directly projected to the jaw and pharynx; the thick axon bundle forming the vagus nerve (X) also passed through the NJC and extended in the posterior direction toward the inner organs; and the axon bundles adjacent to but not passing through the NJC constituted the cranial and spinal components of the accessory nerve (XI).

We then focused on the whole-body projection of the vagus nerve, which is closely related to the brain−gut axis and appetite regulation and has therefore recently garnered significant attention.[71] The visualized 3D distribution of the Phox2b expression was analyzed from multiple angles, enabling the differentiation of adjacent nervous system components that were unclear in two-dimensional images such as the vagus nerve, accessory nerve, and sympathetic chain (Figure 4e−g). Particularly, projections of nodose ganglion-arising vagal sensory axons projected toward the developing organ in E14.5 were clearly visualized by Phox2b. Interestingly, vagal innervation varied according to the target organ: in the heart, the relatively thick major projection of the vagus nerve branched and wrapped around the upper part of both atriums, as shown in Figure 4h. In contrast, in the gut, the major axon of the vagus nerve was observed to thin out toward the end, adjacent to the net-like structure of the enteric nervous system (Figure 4i). Currently, the prevailing methodologies are typically confined to the examination of single organs, restricting comprehensive investigation into the interactions of the latter with neighboring organs. In this regard, whole-body ExM would be especially useful for studying diseases arising from issues in both afferent and efferent neuronal connections. A number of neuronal diseases, including multiple sclerosis,[72] amyotrophic lateral sclerosis,[73] Charcot-Marie-Tooth disease,[74] and Hirschsprung's disease,[75,76] are closely linked to such problems. Visualizing the specific cell types and neural circuits expressing specific proteins at different developmental stages is critical for understanding and treating neurodegenerative diseases.[77−79] The ability of whole-body ExM to visualize the entire body of transgenic embryos from early stages to post-birth offers substantial potential for advancing research in this field.[80]

In ExM imaging of transgenic reporters, a common issue is the loss of endogenous fluorescent signals during the imaging.[81] As prolonged imaging time is required to visualize entire expanded samples, maintaining high signal levels in the processed samples is crucial. To address this need, we tried to amplify the FP signal by applying antibodies to FPs after digestion. Interestingly, the native GFP and tdTomato signals within the expanded samples were successfully amplified even after the digestion, in agreement with previously reported findings.[41] The antigen specificity of the antibodies was well preserved in this post-digestion antibody staining, resulting in patterns consistent with the native FP channel and amplified channel (Figure S15). During the signal amplification with post-digestion antibody staining, we also observed nonspecific binding of antibodies, especially near structures presumed to be nuclei or blood vessels. However, such nonspecific binding was weaker than the true signal, making it easily distinguishable (Figure S16). We then applied post-digestion FP signal amplification in an expanded, half-*Hb9::GFP* embryo at E13.5. Expanded embryos were shrunken back to 2-fold in 1× PBS for post-digestion immunostaining. After staining with the anti-GFP antibody and the corresponding secondary antibody conjugated with Alexa Fluor 546, followed by expansion in 0.1× PBS, Hb9 expression throughout the somatic motor nerves was successfully visualized within the entire body, as shown in Figure 4j,k. In 0.1× PBS, the thickness of a half-embryo at E13.5 was approximately 6 mm. As shown in Figure 4j, GFP signals were amplified uniformly throughout the sample, allowing for the observation of detailed structures from thick motor nerve bundles to their terminating ends with enhanced SNR. This allowed for a detailed examination of how motor projection branches in various directions in the course

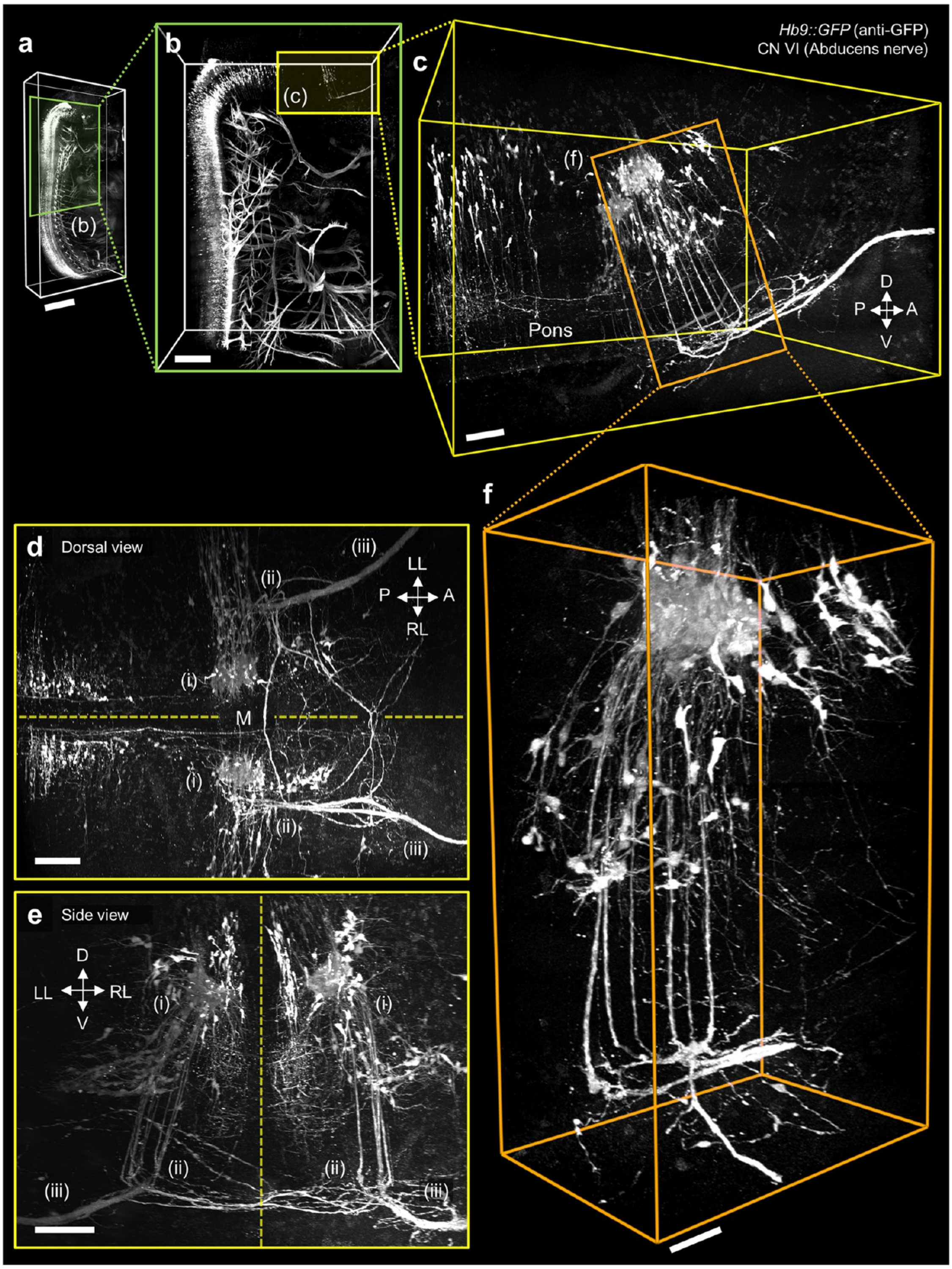

Figure 5. Super-resolution volumetric imaging of the abducens nerve using whole-body ExM. (a) Confocal images of a 3-fold expanded *Hb9::GFP* stained with anti-GFP post digestion. (b) Magnified view of the boxed region in a, but imaged with a 25 ×/0.95 NA objective lens, specifying the location of CN VI in the whole body. (c) Magnified view of the boxed region in b, showing abducens nerves in detail. (d−f) Dorsal and side views of c, showing three major subtracts of CN VI in different views: (i) abducens nucleus and ventrally projecting nerves at rhombomere 5 in the hindbrain; (ii) abducens nerves exiting from the hindbrain; (iii) abducens nerves projecting to the innervation region. (f) Magnified view of the boxed region in b, but imaged with a 60×/1.00 NA objective lens, highlighted the abducens nucleus in the hindbrain and projecting nerves. Direction: A, anterior; P, posterior; D, dorsal; V, ventral; L, lateral; LL, left lateral; RL, right lateral; M, midline. Scale bars: (a) 1 mm; (b) 300 μm; and (c−f) 100 μm. All length scales are presented in pre-expansion dimensions.

of forelimb development, which is a crucial topic for peripheral nerve development and regeneration study (Figure 4l,m).[82] This result, showing that FP signals can be amplified after expansion, implies that transgenically labeled proteins can be imaged post expansion, even if their expression levels are low. Further studies are needed to determine whether other FPs can be labeled post expansion and to identify antibodies that show a lower level of nonspecific binding.

Volumetric Multiscale Imaging of Abducens Nerves Using Whole-Body ExM. We then illustrate the utility of whole-body ExM in imaging the ultrastructure of a specific cranial nerve, the abducens nerve (CN VI). The nuclei of abducens motor neurons are located medially, close to the midline, at rhombomere 5 in the hindbrain.[83,84] The abducens nerve exits ventrally in the hindbrain and turns anteriorly toward the lateral rectus muscles responsible for horizontal eye movements. Therefore, to comprehensively investigate CN VI, imaging techniques that can continuously trace abducens nerves while preserving the original integrity and physical dimensions of these anatomical structures are vital.[85−87] As whole-body ExM enabled the expansion of mouse embryos, it successfully visualized the whole tracks of developing CN VI in a *Hb9::GFP* mouse embryo (E13.5, half-section) with sub-100 nm resolution. The use of a low-magnification objective, such as a 10× objective (NA 0.45), enabled the 3D imaging of a 3-fold-expanded embryonic body with an effective resolution of 195 nm (Figure 5a). Using a 25× objective (NA 0.95), the lateral resolution of 92 nm could be achieved, and thereby, the entire map of developing motor nerves was visualized (Figure 5b). Among these, we focused on the abducens nerves in the region of the hindbrain, as shown in Figure 5c−e. Using a high-magnification objective (60×) with an NA above 1.0, a lateral resolution of 88 nm could be achieved and the 3D morphologies and arrangements of abducens neurons, including the abducens nucleus and their axonal projections, were clearly resolved (Figure 5f).

Such pan-length-scale imaging of the whole mouse embryo would enable the study of changes in the axon morphologies and underlying molecular changes in a single model animal. For example, for a large number of neurological disorders, changes in the shape, size, and numbers of axons in response to genetic and pharmacological perturbations of axon guidance have been observed.[88,89] A transmission electron microscope (TEM) has been used as a gold standard method for studying such structural changes in axons.[90−92] Various TEM investigations have reported that morphological measures vary depending on the type and stage of the neuronal disease.[93−95] Whole-body ExM enables super-resolution 3D imaging of the specific neuronal tracks of mouse embryos, providing more comprehensive insight into diseases.

When whole-body ExM is implemented, it is necessary to take into account the imaging time and systems for the expanded whole animals. Commercially available high NA objectives with a long working distance (e.g., 25× NA 0.95, WD 8 mm)[96] would give an effective resolution of 67 nm when used to image 4.5-fold expanded specimens. Using this objective, the imaging of a 4-fold-expanded whole 6 dpf zebrafish larva and a half sagittal section of an E13.5 mouse embryo would take 2 days and three months, respectively. Depending on the required resolution, expanded specimens could be reversibly shrunk in a buffer containing salt before being imaged.[97] Completely imaging a 2-fold-expanded half mouse embryo with the same objective at an effective resolution of 134 nm could require 11 days. This resolution is high enough to resolve the 3D morphologies of cellular organelles, such as mitochondria and individual axons in the axon bundles. The use of recently developed microscopy systems that can image a larger field of view could reduce the overall imaging time by half.[98] Further reduction in imaging time could be achieved by using fast-evolving light-sheet microscopy techniques, which can acquire high-resolution images at a higher throughput.[32,99]

CONCLUSIONS

In this work, we introduced a state-of-the-art ExM technique, whole-body ExM, which enables the 3D, nanoscale resolution imaging of anatomical structures, proteins, and genetically encoded FPs across the entire body of mice by expanding them 4-fold. In the development of whole-body ExM, we demonstrated that a cyclic digestion process allows for the uniform expansion of mouse embryos, even those with bones and cartilage. Whole-body ExM is both easily applicable and adaptable for mice at a wide range of developmental stages, encompassing a broad spectrum of hard tissue contents, including that of neonatal mice. Whole-body ExM's scalability and ease of application, which require only a simple adjustment of the digestion cycles depending on the specimen, could facilitate the application of ExM to more developed mice and diverse vertebral models without the need for further laborious and time-consuming optimization.

We also validated that the fluorescence signals in immunostained and transgenic mouse embryos are well preserved during the whole-body ExM process, underscoring its usefulness for studying protein distributions throughout the entire body. The compatibility of whole-body ExM with molecular labeling techniques makes it highly attractive for studying the morphological changes of organs and cellular organelles as well as changes in the long processes of specific neurons, with a 60 nm resolution in transgenic models. For example, when applied to a SLICK (Single-neuron labeling with inducible Cre-mediated knockout) mouse line,[100] whole-body ExM would visualize the distribution and morphologies of mitochondria, as well as their interactions with other organelles, in specific neurons from the cortical layers to the spine over a centimeter scale.[97] In addition, *Fzf2*-Cre driver lines crossed with reporter lines would allow high-resolution tracing of the cerebrospinal tracts during embryonic development.[101] When whole-body ExM is combined with state-of-the-art multiplexed cell labeling techniques, such as Confetti mouse[102] or Brainbow-based mice,[103−105] it would be possible to study early cells' clonal expansion over whole embryos.

Whole-body ExM could be improved in multiple ways. First, whole-body ExM could be used to visualize the sub-10 nm details of protein structures over the entire organism. Recently, expansion factors larger than 4-fold, such as 10- or even 20-fold, have been demonstrated using different hydrogels or through multiround expansion.[19,25,29,35,106] Once combined with such more-than-4-fold expansion techniques, whole-body ExM would enable the study of the entire organism at a molecular resolution. Second, whole-body ExM could be combined with tissue-clearing techniques that enable the rapid immunostaining of thick tissues. Recently, multiple technological breakthroughs, such as delipidation,[9,107] the use of nanobodies,[5] and the optimization of staining conditions depending on antigen densities, fluorophore charges, and temperatures,[10] have accelerated immunostaining, enabling its application to mm-thick specimens,[6,11,108] even whole mice.[109] Other rapid staining techniques that strongly fix specimens and accelerate antibody diffusion by applying electric fields could also be used to stain whole mouse embryos.[110−112] The compatibility of these techniques, as well as many others, with the whole-body ExM protocol, should also be studied.[113,114]

Although whole-body ExM has been successfully applied with various fluorescent labels, further validation is needed to ensure compatibility with high-temperature digestion. The quantitative analysis of fluorescent signals after extended digestion at elevated temperatures has yet to be thoroughly validated. Retention and amplification of fluorescent signals in whole-body ExM-processed samples could be further tested for practical applications in neonatal mice. Another potential limitation when whole-body ExM is applied to larger samples is that the current hydrogel may not provide sufficient physical support after expansion. Its limited mechanical properties often make bulky specimens, such as neonatal mice, fragile and prone to damage during handling. Fortunately, various recipes have been explored to optimize ExM, e.g., enhance imaging resolution,[26,29,115] and improve mechanical properties.[116] It would be valuable to investigate whether the proposed improvements in the hydrogel composition could enhance mechanical properties while remaining compatible with whole-body ExM.

EXPERIMENTAL SECTION

Materials. All chemicals and antibodies were obtained from commercial suppliers; detailed information is provided in Table S1. The concentrations of the labeling agents, including antibodies and fluorophore NHS esters, are listed in Table S2.

Biological Sample Preparation. *Ethical Regulations.* All experimental methods involving mice and zebrafish were approved by the Korea Advanced Institute of Science and Technology Institutional Animal Care and Use Committee (KAIST-IACUC), the Korea Institute of Science and Technology Institutional Animal Care and Use Committee (KIST-IACUC), the Gwangju Institute of Science and Technology Institutional Animal Care and Use Committee (GIST-IACUC), the Seoul National University Institutional Animal Care and Use Committee (SNU-IACUC), the Chungnam National University Institutional Animal Care and Use Committee (CNU-IACUC), and the Korea Research Institute of Bioscience and Biotechnology (KRIBB)-IACUC.

Mouse Brain Slice Preparation. C57BL/6J mice aged 6–8 weeks were used for organ harvesting. After anesthetization with isoflurane, the mice were transcardially perfused with 1× phosphate-buffered saline (PBS), followed by perfusion with 4% paraformaldehyde (PFA) in 1× PBS. Brains were harvested and fixed in 4% PFA in 1× PBS at 4 °C for 2–6 h. Fixed brains were then sliced to a thickness of 150 μm with a vibratome (VT1000S; Leica, Wetzlar, Germany).

Mouse Embryo Preparation. Pregnant C57BL/6J mice were deeply anesthetized and euthanized with isoflurane before surgery. Mouse embryos were isolated from pregnant mice. Mouse embryos older than E15.5 were deeply anesthetized and euthanized with isoflurane before fixation. For E18.5, the mouse embryos were skinned to facilitate the diffusion of the fixative. Isolated embryos were fixed with 4% PFA in 1× PBS at 4 °C for 12–24 h, depending on the size of the body. Embryos were used as sliced, half-embryo, or whole embryos. For sliced and half-embryo preparation, fixed mouse embryos were embedded in 4–6% (w/w) low-gelling-temperature agarose and then either sliced to a thickness of 500–1000 μm or cut into sagittal sections along the midline of the body.

Neonatal Mice Preparation. Neonatal mice were deeply anesthetized and euthanized with isoflurane. The neonatal mice were transcardially perfused with 1× PBS, followed by perfusion with 4% PFA in 1× PBS. After perfusion, the neonatal mice were skinned to facilitate the diffusion of the fixative. Skinned neonatal mice were then post-fixed with 4% PFA in 1× PBS at 4 °C for 24–48 h, depending on the size of the body. The sectioning of the sample was conducted as previously described.

Zebrafish Larvae Preparation. Euthanized *D. rerio* aged 6 dpf were fixed with 4% PFA in 1× PBS at 4 °C overnight. The fixed larvae were stored in 1× PBS with 0.1 M glycine and 0.01% (w/w) sodium azide at 4 °C before use.

General Whole-Body ExM Protocol. *Note for the Whole-Body ExM Protocol.* In this section, we describe the general protocol of whole-body ExM, which is based on the cyclic digestion process. An example of the whole-body ExM workflow with 5.5 cycles of cyclic digestion is illustrated in Figure S17. Experiments using whole-body ExM were conducted as follows unless otherwise specified in the manuscript. The volume of the digestion solutions was adjusted depending on the size of the samples. Total digestion cycles (n) is an experimentally determined value. We also note that the purity and freshness of the reagents and buffers, especially those used for fixation, anchoring, gelation, and digestion, would also affect the n; depending on the purity and freshness of the reagents, it may be necessary to increase the n. Enzyme activity and quality control are discussed in detail in Supporting Note 5. Table S3 summarizes products offering similar levels of purity, stability, and activity to those used in this study.

Whole-Body ExM Protocol. Hydrogel Embedding. All processes before gel synthesis were conducted at 4 °C with gentle shaking. Fixed samples were permeabilized with 0.1–0.2% PBST (0.1–0.2% Triton X-100 in 1× PBS) for 1–14 days. Samples were incubated in 0.1 mg/mL AcX in 0.1% PBST 1–2 times for 12–24 h each time: Embryo slices and whole larval zebrafish were treated once; half and whole embryos were treated 1–2 times depending on the size of the sample. Samples were washed with 0.1% PBST three times for 30 min each time. The samples were incubated in a freshly prepared gelation solution (8.625% [w/w] sodium acrylate, 2.5% [w/w] acrylamide, 0.15% [w/w] *N*,*N*-methylenebis(acrylamide) [BIS], 0.2% [w/w] 2,2′-azobis[2-(2-imidazolin-2-yl)propane] dihydrochloride [VA-044], 0.05–0.1% [w/w] Triton X-100, 2 M NaCl, 1× PBS) four times for 12 h each time. After the incubation, the samples were placed between two glass slides along with spacers matching the thickness of each sample and then incubated at 45 °C for 12–24 h in a humidified chamber.

Cyclic Digestion. After gel synthesis, the excess gel around the sample was trimmed off using a razor blade. The gel-embedded samples were then homogenized via *n*-cycles of cyclic digestion at 37 °C with gentle shaking. One cycle of the digestion process involved being treated twice with proteinase K and then twice with collagenase mixture: samples were first digested with 16 U/mL proteinase K in proteinase K digestion buffer (1 mM ethylenediaminetetraacetic acid [EDTA], 50 mM Tris-HCl [pH 8.0], 0.5% Triton X-100, 2 M NaCl) twice for 12 h each time; samples were then washed with collagenase digestion buffer (1× HBSS [pH 6.7], 3 mM $CaCl_2$) three times for 30 min each time; washed samples were then digested with a collagenase mixture (2 mg/mL [minimum 400 U/mL] of collagenase type I, collagenase type II, and collagenase type IV) in collagenase digestion buffer twice for 12 h each time. Washing was performed only in the transition from proteinase K digestion to collagenase mixture digestion in order to remove EDTA contained in the proteinase K digestion buffer. If needed, fluorophore NHS ester staining was conducted as follows: after the two proteinase K digestion steps of the first digestion cycle, samples were washed with staining buffer (0.1% Triton X-100, 2 M NaCl, 1× PBS) three times for 30 min each time. Washed samples were incubated with diluted fluorophore NHS ester in the staining buffer at 4 °C (Table S2 summarizes the final concentration of the fluorophore NHS esters). Stained samples were then subjected to further digestion. The digestion process always ended with treatment twice with proteinase K, corresponding to the 0.5 cycle.

Expansion. After digestion, fully homogenized samples were treated with an excess volume of decalcification solution (0.3 M EDTA [pH 8.0], 2 M NaCl, 0.1% Triton X-100) at 4 °C four times for 12 h each time. The samples were then washed with an excess volume of deionized water and kept in fresh deionized water overnight for expansion until the size of the hydrogels plateaued.

Whole-Body ExM for E18.5 Mouse Embryos and Neonatal Mice. The general whole-body ExM protocol was also used for expanding E18.5 mouse embryos, P2 neonatal mice, and P5 neonatal mice, with a few modifications: the temperature was increased from 37 to 60 °C during the cyclic digestion, and the concentration of proteinase K was decreased from 16 to 8 U/mL. All other conditions remained the same.

Validation of Isotropy. *Microscale Distortion Analysis.* 500 μm-thick E15.5 mouse embryo slices were blocked and permeabilized with NGS blocking buffer (5% normal goat serum [NGS], 0.1% Triton X-100, 1× PBS) for 12 h at 4 °C. Permeabilized samples were incubated with anti-TuJ1 antibodies in NGS blocking buffer for 3 days at 4 °C, followed by washing in the NGS blocking buffer six times for 0.5−1 h each time. Samples were then incubated with fluorophore-conjugated secondary antibodies in NGS blocking buffer for 3 days at 4 °C, followed by washing in NGS blocking buffer six times for 0.5−1 h each time. Pre-expansion imaging of embryo slices was conducted by using a spinning disk confocal microscope. After imaging, samples were subjected to the whole-body ExM process, as described in the General Whole-Body ExM Protocol, with 5.5 cycles of digestion. After expansion, samples were imaged with a spinning disk confocal microscope to obtain post expansion images. The RMSE was measured in a similar way to that described in a previous study.[24] Briefly, pre-expansion and post expansion images were registered in the open-source software *Elastix*, using rigid (similarity) and nonrigid (b-spline) transformations to quantify distortions. After the registration, deformation vector fields were calculated by using *Elastix* and *Transformix* as described in the reference. A total of 11 ROIs from three different samples were used for RMSE quantification.

Nanoscale Distortion Analysis. Blocking, permeabilization, antibody staining against CCP, pre-expansion imaging (at this time, to enable the more precise imaging of nanostructures of CCPs before expansion, we used LSM980 in Airyscan2 mode), the whole-body ExM process, and post-expansion imaging were conducted on 500 μm-thick E15.5 mouse embryo slices as described under Microscale Distortion Analysis. To quantify the expansion factor, the radii of single CCPs and the distance between nearby CCPs were measured pre- and post expansion. To be specific, ROIs were extracted for each pit or nearby pits. To measure the radii of a single pit, the intensity profile along the pit was extracted with a line width covering the whole pit using *ImageJ*, a double-Gaussian-fitted line was obtained by *Origin*, and the distance between the peaks was measured. Similarly, the distance between nearby pits was calculated by the distance between the peaks of the double-Gaussian-fitted line obtained from the line profile between nearby pits, with a line-width covering the nearby pits (data points that showed errors during double-Gaussian fitting in *Origin*, such as those without two distinct peaks or with negative peak values, were excluded from the quantification).

Validation of Antibody Compatibility. *Antibody Staining of Mouse Embryo Slices and the Whole-Body ExM Process.* 500 μm-thick E15.5 mouse embryo slices were blocked and permeabilized with NGS blocking buffer for 24 h at 4 °C. Permeabilized samples were incubated with primary antibodies in NGS blocking buffer for at least 48 h at 4 °C, after which they were washed in NGS blocking buffer three times for 30 min each time. The samples were then incubated with secondary antibodies in NGS blocking buffer for 24 h at 4 °C and then washed in NGS blocking buffer three times for 1 h each time. After immunostaining, samples were subjected to the whole-body ExM process (as described in the General Whole-Body ExM Protocol) with 5.5 cycles of digestion.

Antibody Staining of Whole Embryos and the Whole-Body ExM Process. E12.5 *Hb9::GFP* mouse embryos were blocked and permeabilized with NDS blocking buffer (5% NDS, 0.2% Triton X-100, 1× PBS, 0.02% sodium azide) for 3 days at 37 °C. Permeabilized samples were incubated with primary antibodies in NDS blocking buffer for at least 7 days at 37 °C, then washed in NDS blocking buffer 12 times for 1−2 h each time. Samples were then incubated with secondary antibodies in NDS blocking buffer for at least 4 day at 37 °C, then washed in NDS blocking buffer 12 times for 1−2 h each time. After immunostaining, samples were subjected to the whole-body ExM process (as described in the General Whole-Body ExM protocol).

Signal Amplification. *Signal Amplification Using Anti-Alexa Fluor 488 Antibody and Quantitative Analysis.* A total of nine different antibodies were tested in parallel. Brain slices were blocked and permeabilized with an NGS or NDS blocking buffer for 2 h. Permeabilized samples were then incubated with primary antibodies in a blocking buffer for 3−9 h at 4 °C and then washed in 0.1% PBST three times for 30 min each time. Alexa Fluor 488-conjugated-secondary antibodies diluted in blocking buffer were then added for 3−9 h at 4 °C followed by washing in 0.1% PBST three times for 30 min each time. The anchoring and gelation of brain slices were performed as previously described in the proExM protocol.[23] Gel-embedded brain slices were then digested with 16 U/mL proteinase K in proteinase K digestion buffer four times, each lasting 12 h at 37 °C. After prolonged digestion, samples were expanded ∼2-fold in 1× PBS and imaged with a confocal microscope. After the preamplification imaging, samples were then further digested with a collagenase mixture (2 mg/mL [minimum 400 U/mL] of collagenase type I, collagenase type II, and collagenase type IV) in collagenase digestion buffer twice for 12 h each time at 37 °C, followed by incubation with 16 U/mL of proteinase K in proteinase K digestion buffer six times, each lasting 12 h at 37 °C. After further digestion, samples were immunostained with anti-Alexa Fluor 488 antibodies diluted in 0.1% PBST for 24 h and Alexa Fluor 488-conjugated antirabbit secondary antibodies diluted in 0.1% PBST for 24 h to boost the fluorescent signal. Then, each staining was washed six times with 0.1% PBST for 30 min. After the signal amplification, samples were subjected to post-amplification imaging under the same imaging conditions in 1× PBS. The signal intensity was measured at the same location from the pre-signal amplification and post-signal amplification images of each sample, and the relative signal intensity after signal amplification with respect to the pre-signal amplification was calculated. In all nine specimens, the fluorescence signal intensity of Alexa Fluor 488 before and after amplification was measured at the same locations. This quantification was repeated at 30 locations in each sample. One brain slice was used for each antibody.

Post-digestion Signal Amplification Using Anti-FP Antibodies in Transgenic Mouse Embryos. Expanded samples were incubated in an NDS blocking buffer for 6 h at 37 °C for shrinking and blocking. Samples were incubated with anti-FP antibodies (either anti-RFP or anti-GFP) in NDS blocking buffer for at least 3 days at 37 °C, then washed in 0.2% PBST at least 12 times for 1−2 h each time. Samples were then incubated with secondary antibodies in NDS blocking buffer for at least 3 days at 37 °C, then washed in 0.2% PBST at least 12 times for 1−2 h each time.

Fluorophore NHS-Ester Staining Pattern Analysis. *Immunostaining of Mouse Brain Slices.* Brain slices were blocked and permeabilized with an NGS blocking buffer for 1−3 h. For brain slices that were imaged for actin, the permeabilized brains were stained with fluorescein phalloidin in NGS blocking buffer overnight at 4 °C and then washed in 0.1% PBST three times for 30 min each time. Permeabilized samples were then incubated with primary antibodies in NGS blocking buffer for at least 6 h at 4 °C and then washed in 0.1% PBST three times for 30 min each time. Secondary antibodies diluted in NGS blocking buffer were then added for at least 6 h at 4 °C and then washed in 0.1% PBST three times for 30 min each time.

In Vivo Mitochondria Labeling. To label mitochondria in parvalbumin (PV)-positive neurons, *Cre*-dependent adeno-associated virus (AAV) expressing mScarlet followed by mitochondrial matrix-targeting sequence was injected into the PV-*Cre* mouse line (B6.129P2-*Pvalb*$^{tm1(cre)Arbr}$/J), as follows: the mice were anesthetized with isoflurane and placed in a stereotaxic frame. Then, 100 nL of a 10:1 cocktail of AAV-Jx-synaptophysin-mVenus-T2A-mito-mScarlet was injected into the subthalamic nucleus (STN, AP: + 1.62 mm; ML: 1.65 mm; DV: −4.45, −4.55, and −4.65 mm) at a speed of 40 nL/min. Ten days after an AAV injection, mouse brains were harvested and fixed as described above in Biological Sample Preparation.

ProExM and Fluorophore NHS-Ester Staining in Mouse Brain Slices. Permeabilization, AcX treatment, gelation, and digestion of mouse brain slices were performed as previously described in the proExM protocol.[23] Fully digested brain slices were stained with diluted fluorophore NHS ester in 0.1% PBST for at least 6 h at 4 °C and then washed in 0.1% PBST three times for 30 min each time. Stained samples were then expanded in deionized water and imaged to analyze staining patterns.

Imaging and Data Processing. *Sample Mounting and Imaging.* For the imaging of expanded specimens, the hydrogels were attached to poly-L-lysine-coated glasses to prevent hydrogel drifting during imaging. Specimens were imaged using a spinning disk confocal microscope (Olympus BX51WI microscope equipped with Andor Dragonfly 200 and an Andor Zyla 4.2 sCMOS) or laser scanning confocal microscope (Nikon Eclipse Ti2-E microscope equipped with Nikon C2+; or ZEISS LSM980). The objectives used were 63× 1.4 NA oil immersion lens, 60× 1.00 NA water immersion lens, 40× 1.15 NA water immersion lens, 25× 0.95 NA water immersion lens, 10× 0.45 NA air lens, 10× 0.4 NA air lens, and 4× 0.2 NA air lens.

Intensity Adjustment. The images shown in Figure 1l−p were thresholded to zero using a specific threshold value to more clearly visualize the expanded embryos rather than the surrounding gels. Images shown in Figure 3b−n were thresholded to zero using a specific threshold value to enhance the visibility. Images shown in Figures 4j−l and 5a−f were thresholded to zero using specific threshold values to remove signals from nonspecific binding, which is discussed in Figure S16.

Shading Correction. The following image processing pipelines were applied to the images in Figures 1l,1n and 4c−g. A custom Python script was used to apply the BaSiC algorithm[117] for flat-field estimation and shading correction on 3D image stacks in the Imaris file format (.ims). To ensure even illumination after correction across sections within a single image set consisting of multiple 3D stacks, 40 image slices (1024 px × 1024 px each) were sampled evenly from each 3D image stack along the z-direction. BaSiC with default parameters was used to estimate the flat-field profiles from the sampled slices. For multichannel images, a single image channel with the densest labeling was used to estimate the flat-field for all other channels. A single estimated flat-field profile was used to correct shading in all 3D image stacks, with correction applied to each image slice along the z-directions independently. Corrected image stacks were saved as. ims files for further processing, including multistack stitching and visualization in Imaris 9.5.

Denoising and Deconvolution. The following image processing pipelines were applied to the images in Figure 4b,4j,k. Images were first denoised using SUPPORT,[118] which removed the Poisson−Gaussian noise in the images by learning and utilizing the spatial and temporal dependence among the pixel values (publicly available on https://github.com/NICALab/SUPPORT). The training process involved 150 000 iterations of updates with a batch size of 64 and utilized patches of size $3(x) \times 128(x) \times 128(y)$. The SUPPORT network had a receptive field size of $3(z) \times 146(x) \times 146(y)$ and a blind spot size of $1(z) \times 1(x) \times 1(y)$. Thereafter, the z-stack images were deconvolved by using the Richardson−Lucy algorithm and a theoretical point-spread function. All denoising was performed on a workstation equipped with two Intel Xeon Gold 6226R CPUs, 128 GiB of RAM, and an NVIDIA GeForce RTX 4090 GPU, and the rest was performed on a workstation equipped with an Intel i7-11700K CPU and 128 GiB of RAM.

ASSOCIATED CONTENT

Data Availability Statement

All data needed to evaluate the conclusions in the paper are present in the paper and/or the Supporting Information. Additional relevant data can be obtained from the corresponding authors upon reasonable request.

Supporting Information

The Supporting Information is available free of charge at https://pubs.acs.org/doi/10.1021/acsnano.4c14791.

Detailed analysis of the fluorophore NHS-ester staining patterns, effects of collagenase mixture treatment, and quantitative signal amplification, as well as whole-body ExM imaging of zebrafish larvae and newborn mice, and examples of whole-body ExM workflows; supporting Figures 1−17; supporting Notes 1−5; and supporting Tables 1−3 (PDF)

Revised figures (ZIP)

AUTHOR INFORMATION

Corresponding Authors

Young-Gyu Yoon − *School of Electrical Engineering, Korea Advanced Institute of Science and Technology, Daejeon 34141, Republic of Korea; KAIST Institute for Health Science and Technology, Daejeon 34141, Republic of Korea;* Email: ygyoon@kaist.ac.kr

Jae-Byum Chang − *Department of Materials Science and Engineering, Korea Advanced Institute of Science and Technology, Daejeon 34141, Republic of Korea; Department of Biological Sciences, Korea Advanced Institute of Science and Technology, Daejeon 34141, Republic of Korea; Bioimaging Data Curation Center, Seoul 03760, Republic of Korea;* orcid.org/0000-0002-3554-5647; Email: jbchang03@kaist.ac.kr

Authors

Jueun Sim − *Department of Materials Science and Engineering, Korea Advanced Institute of Science and Technology, Daejeon 34141, Republic of Korea;* orcid.org/0000-0003-4849-4591

Chan E. Park − *Department of Materials Science and Engineering, Korea Advanced Institute of Science and Technology, Daejeon 34141, Republic of Korea*

In Cho − *Department of Materials Science and Engineering, Korea Advanced Institute of Science and Technology, Daejeon 34141, Republic of Korea*

Kyeongbae Min − *Department of Biomedical Engineering, Sungkyunkwan University, Suwon 21102, Republic of Korea*

Minho Eom − *School of Electrical Engineering, Korea Advanced Institute of Science and Technology, Daejeon 34141, Republic of Korea*

Seungjae Han − *School of Electrical Engineering, Korea Advanced Institute of Science and Technology, Daejeon 34141, Republic of Korea*

Hyungju Jeon − *Brain Science Institute, Korea Institute of Science and Technology, Seoul 02792, Republic of Korea*

Eun-Seo Cho − *School of Electrical Engineering, Korea Advanced Institute of Science and Technology, Daejeon 34141, Republic of Korea*

Yunjeong Lee − *School of Life Sciences, Gwangju Institute of Science and Technology, Gwangju 61005, Republic of Korea*

Young Hyun Yun − *Department of Anatomy and Cell Biology, Seoul National University College of Medicine, Seoul 03080, Republic of Korea*

Sungho Lee − *School of Biological Sciences, Seoul National University, Seoul 08826, Republic of Korea*

Deok-Hyeon Cheon − *Department of Anatomy and Cell Biology, Seoul National University College of Medicine, Seoul 03080, Republic of Korea*

Jihyun Kim − *Brain Science Institute, Korea Institute of Science and Technology, Seoul 02792, Republic of Korea; Department of Integrated Biomedical and Life Sciences, College of Health Sciences, Korea University, Seoul 02841, Republic of Korea*

Museong Kim − *Department of Biological Sciences, Korea Advanced Institute of Science and Technology, Daejeon 34141, Republic of Korea*

Hyun-Ju Cho − *Microbiome Convergence Research Center, Korea Research Institute of Bioscience and Biotechnology, Daejeon 34141, Republic of Korea*

Ji-Won Park − *Department of Biology, Chungnam National University, Daejeon 34134, Republic of Korea*

Ajeet Kumar − *Department of Biological Sciences, Korea Advanced Institute of Science and Technology, Daejeon 34141, Republic of Korea*

Yosep Chong − *Department of Hospital Pathology, Uijeongbu St. Mary's Hospital, College of Medicine, The Catholic University of Korea, Uijeongbu 11765, Republic of Korea*

Jeong Seuk Kang − *John A. Paulson School of Engineering and Applied Sciences, Harvard University, Cambridge, Massachusetts 02138, United States*

Kiryl D. Piatkevich − *School of Life Sciences and Westlake Laboratory of Life Sciences and Biomedicine, Westlake University, Hangzhou 310024 Zhejiang, China; Institute of Basic Medical Sciences, Westlake Institute for Advanced Study, Hangzhou 310024 Zhejiang, China*

Erica E. Jung − *Department of Mechanical and Industrial Engineering, The University of Illinois at Chicago, Chicago, Illinois 60607, United States*

Du-Seock Kang − *Graduate School of Medical Science and Engineering, Korea Advanced Institute of Science and Technology, Daejeon 34141, Republic of Korea*

Seok-Kyu Kwon − *Brain Science Institute, Korea Institute of Science and Technology, Seoul 02792, Republic of Korea; Division of Bio-Medical Science and Technology, KIST School, Korea University of Science and Technology, Seoul 02792, Republic of Korea*

Jinhyun Kim − *Brain Science Institute, Korea Institute of Science and Technology, Seoul 02792, Republic of Korea; Department of Integrated Biomedical and Life Sciences, College of Health Sciences, Korea University, Seoul 02841, Republic of Korea; KIST-SKKU Brain Research Center, SKKU Institute for Convergence, Sungkyunkwan University, Suwon 16419, Republic of Korea*

Ki-Jun Yoon − *Department of Biological Sciences, Korea Advanced Institute of Science and Technology, Daejeon 34141, Republic of Korea*

Jeong-Soo Lee − *Microbiome Convergence Research Center, Korea Research Institute of Bioscience and Biotechnology, Daejeon 34141, Republic of Korea; KRIBB School, University of Science and Technology, Daejeon 34141, Republic of Korea*

Cheol-Hee Kim − *Department of Biology, Chungnam National University, Daejeon 34134, Republic of Korea*

Myunghwan Choi − *School of Biological Sciences, Seoul National University, Seoul 08826, Republic of Korea*

Jin Woo Kim − *Department of Biological Sciences, Korea Advanced Institute of Science and Technology, Daejeon 34141, Republic of Korea*

Mi-Ryoung Song − *School of Life Sciences, Gwangju Institute of Science and Technology, Gwangju 61005, Republic of Korea*

Hyung Jin Choi − *Department of Anatomy and Cell Biology, Seoul National University College of Medicine, Seoul 03080, Republic of Korea; Department of Brain and Cognitive Sciences, Seoul National University, Seoul 08826, Republic of Korea*

Edward S. Boyden − *Howard Hughes Medical Institute, Cambridge, Massachusetts 02138, United States; McGovern Institute, Massachusetts Institute of Technology, Cambridge, Massachusetts 02139, United States; Departments of Brain and Cognitive Sciences, Media Arts and Sciences, and Biological Engineering, Massachusetts Institute of Technology, Cambridge, Massachusetts 02139, United States*

Complete contact information is available at: https://pubs.acs.org/10.1021/acsnano.4c14791

Author Contributions

○○○J.S., C.E.P., and I.C. contributed equally to this work. J.S., C.E.P., and I.C. wrote the manuscript and created the graphics. J.S., C.E.P., I.C., and K.M. performed the experiments and analyses. M.E., S.H., and E.-S.C. processed volumetric images for denoising. H.J. processed large images for fine stitching. Y.L., Y.H.Y., S.L., D.-H.C., J.K., M.K., and A.K. prepared the mouse embryos and performed data analysis. E.-S.C., H.-J.C., and J.-W.P. prepared zebrafish larvae and performed data analysis. Y.C. analyzed the anatomical structures of expanded mice. J.S.K., K.D.P., and E.E.J. contributed to whole-zebrafish imaging and experimental design. D.-S.K. contributed to whole-mount immunostaining and designed an experimental process with mouse embryos. S.-K.K. prepared in vivo mitochondria-labeled mouse brains. M.C., J.W.K., M.-R.S., H.J.C., and K.-J.Y. analyzed the neuronal structures of expanded mouse embryos. J.-S.L. and C.-H.K. analyzed the anatomical structures of expanded larvae. E.S.B. supervised the imaging of the whole larvae. Y.-G.Y. supervised image processing. J.-B.C. supervised this work. All authors participated in contributing to the text and the content of the manuscript, including revisions and edits.

Notes

The authors declare the following competing financial interest(s): J.-B.C., J.S., C.E.P., I.C., K.M., and Y.-G.Y. are inventors on multiple patents related to whole-body ExM and fluorophore NHS-ester staining, with each having varying levels of involvement across these patents. E.S.B. is an inventor on numerous patents relating to ExM, and is a founder of a company exploring commercial applications of ExM. J.-B.C., Y.-G.Y., C.E.P., and I.C. are co-founders of a company specializing in diverse imaging services.

Associated Contents J.S.; C.E.P.; I.C.; et al. Nanoscale resolution imaging of the whole mouse embryos and larval zebrafish using expansion microscopy. 2022, bioRxiv. URL: 10.1101/2021.05.18.443629 (accessed December 11, 2024).

ACKNOWLEDGMENTS

This work was supported by the Samsung Research Funding & Incubation Center for Future Technology (SRFC-IT1702-09). Y.-G.Y. acknowledges funding through RS-2023-00209473 from the National Research Foundation of Korea (NRF). J.K. acknowledges funding through 2E32901 from the Korea Institute of Science and Technology Program. E.S.B. acknowledges funding, NIH 1R01EB024261, Good Ventures, Open Philanthropy, Lisa Yang, John Doerr, HHMI, NIH Director's Pioneer Award 1DP1NS087724, and the U.S. Army Research Laboratory and the U.S. Army Research Office under contract/grant number W911NF1510548. H.J.C. acknowledges for funding RS-2024-00404132 from the Korea Health Industry Development Institute. This research was also supported by the Bio & Medical Technology Development Program of the

National Research Foundation (NRF) funded by the Korean government (MSIT) (RS-2022-NR068424). The authors acknowledge Prof. Taeyun Ku and Young Seo Kim for their help with imaging. The authors also acknowledge Prof. Taejoon Kwon for helpful discussions. The authors thank Prof. Woong Sun, Prof. Minah Suh, Prof. Han Kyoung Choe, Su Yeon Kim, Dr. Jang Soo Yuk, Dr. Yun-Mi Jeong, and Dr. Hoi-Khoanh Giong. The authors acknowledge Prof. Hyuk Wan Ko, Dr. Rose G. Long, Prof. Robert Parton, and Prof. Tanya T. Whitfield for insightful discussions.

REFERENCES

(1) Susaki, E. A.; Ueda, H. R. Whole-Body and Whole-Organ Clearing and Imaging Techniques with Single-Cell Resolution: Toward Organism-Level Systems Biology in Mammals. *Cell Chem. Biol.* **2016**, *23* (1), 137−157.

(2) Ueda, H. R.; Ertürk, A.; Chung, K.; Gradinaru, V.; Chédotal, A.; Tomancak, P.; Keller, P. J. Tissue Clearing and Its Applications in Neuroscience. *Nat. Rev. Neurosci.* **2020**, *21* (2), 61−79.

(3) Richardson, D. S.; Guan, W.; Matsumoto, K.; Pan, C.; Chung, K.; Ertürk, A.; Ueda, H. R.; Lichtman, J. W. Tissue Clearing. *Nat. Rev. Methods Primers* **2021**, *1* (1), 84.

(4) Liu, Z.; Keller, P. J. Emerging Imaging and Genomic Tools for Developmental Systems Biology. *Dev Cell* **2016**, *36* (6), 597−610.

(5) Cai, R.; Pan, C.; Ghasemigharagoz, A.; Todorov, M. I.; Förstera, B.; Zhao, S.; Bhatia, H. S.; Parra-Damas, A.; Mrowka, L.; Theodorou, D.; Rempfler, M.; Xavier, A. L. R.; Kress, B. T.; Benakis, C.; Steinke, H.; Liebscher, S.; Bechmann, I.; Liesz, A.; Menze, B.; Kerschensteiner, M.; Nedergaard, M.; Ertürk, A. Panoptic Imaging of Transparent Mice Reveals Whole-Body Neuronal Projections and Skull−Meninges Connections. *Nat. Neurosc.* **2019**, *22* (2), 317−327.

(6) Pan, C.; Cai, R.; Quacquarelli, F. P.; Ghasemigharagoz, A.; Lourbopoulos, A.; Matryba, P.; Plesnila, N.; Dichgans, M.; Hellal, F.; Ertürk, A. Shrinkage-Mediated Imaging of Entire Organs and Organisms Using UDISCO. *Nat. Methods* **2016**, *13* (10), 859−867.

(7) Tainaka, K.; Kubota, S. I.; Suyama, T. Q.; Susaki, E. A.; Perrin, D.; Ukai-Tadenuma, M.; Ukai, H.; Ueda, H. R. Whole-Body Imaging with Single-Cell Resolution by Tissue Decolorization. *Cell* **2014**, *159* (4), 911−924.

(8) Yang, B.; Treweek, J. B.; Kulkarni, R. P.; Deverman, B. E.; Chen, C. K.; Lubeck, E.; Shah, S.; Cai, L.; Gradinaru, V. Single-Cell Phenotyping within Transparent Intact Tissue through Whole-Body Clearing. *Cell* **2014**, *158* (4), 945−958.

(9) Renier, N.; Wu, Z.; Simon, D. J.; Yang, J.; Ariel, P.; Tessier-Lavigne, M. IDISCO: A Simple, Rapid Method to Immunolabel Large Tissue Samples for Volume Imaging. *Cell* **2014**, *159* (4), 896−910.

(10) Susaki, E. A.; Shimizu, C.; Kuno, A.; Tainaka, K.; Li, X.; Nishi, K.; Morishima, K.; Ono, H.; Ode, K. L.; Saeki, Y.; Miyamichi, K.; Isa, K.; Yokoyama, C.; Kitaura, H.; Ikemura, M.; Ushiku, T.; Shimizu, Y.; Saito, T.; Saido, T. C.; Fukayama, M.; Onoe, H.; Touhara, K.; Isa, T.; Kakita, A.; Shibayama, M.; Ueda, H. R. Versatile Whole-Organ/Body Staining and Imaging Based on Electrolyte-Gel Properties of Biological Tissues. *Nat. Commun.* **2020**, *11* (1), 1982.

(11) Belle, M.; Godefroy, D.; Couly, G.; Malone, S. A.; Collier, F.; Giacobini, P.; Chédotal, A. Tridimensional Visualization and Analysis of Early Human Development. *Cell* **2017**, *169* (1), 161−173.

(12) Jing, D.; Zhang, S.; Luo, W.; Gao, X.; Men, Y.; Ma, C.; Liu, X.; Yi, Y.; Bugde, A.; Zhou, B. O.; Zhao, Z.; Yuan, Q.; Feng, J. Q.; Gao, L.; Ge, W. P.; Zhao, H. Tissue Clearing of Both Hard and Soft Tissue Organs with the PEGASOS Method. *Cell Res.* **2018**, *28* (8), 803−818.

(13) Rawson, S. D.; Maksimcuka, J.; Withers, P. J.; Cartmell, S. H. X-Ray Computed Tomography in Life Sciences. *BMC Biol.* **2020**, *18* (1), 21.

(14) Mulcahy, B.; Witvliet, D.; Holmyard, D.; Mitchell, J.; Chisholm, A. D.; Meirovitch, Y.; Samuel, A. D. T.; Samuel, A. D. T.; Zhen, M. A Pipeline for Volume Electron Microscopy of the Caenorhabditis Elegans Nervous System. *Front. Neural Circuits* **2018**, *12*, 94.

(15) Kasthuri, N.; Hayworth, K. J.; Berger, D. R.; Schalek, R. L.; Conchello, J. A.; Knowles-Barley, S.; Lee, D.; Vázquez-Reina, A.; Kaynig, V.; Jones, T. R.; Roberts, M.; Morgan, J. L.; Tapia, J. C.; Seung, H. S.; Roncal, W. G.; Vogelstein, J. T.; Burns, R.; Sussman, D. L.; Priebe, C. E.; Pfister, H.; Lichtman, J. W. Saturated Reconstruction of a Volume of Neocortex. *Cell* **2015**, *162* (3), 648−661.

(16) Hildebrand, D. G. C.; Cicconet, M.; Torres, R. M.; Choi, W.; Quan, T. M.; Moon, J.; Wetzel, A. W.; Scott Champion, A.; Graham, B. J.; Randlett, O.; Plummer, G. S.; Portugues, R.; Bianco, I. H.; Saalfeld, S.; Baden, A. D.; Lillaney, K.; Burns, R.; Vogelstein, J. T.; Schier, A. F.; Lee, W. C. A.; Jeong, W. K.; Lichtman, J. W.; Engert, F. Whole-Brain Serial-Section Electron Microscopy in Larval Zebrafish. *Nature* **2017**, *545* (7654), 345−349.

(17) Chen, F.; Tillberg, P. W.; Boyden, E. S. Expansion Microscopy. *Science* **2015**, *347* (6221), 543−548.

(18) Cho, I.; Seo, J. Y.; Chang, J. Expansion Microscopy. *J. Microsc.* **2018**, *271* (2), 123−128.

(19) M'Saad, O.; Bewersdorf, J. Light Microscopy of Proteins in Their Ultrastructural Context. *Nat. Commun.* **2020**, *11* (1), 3850.

(20) Gambarotto, D.; Zwettler, F. U.; Le Guennec, M.; Schmidt-Cernohorska, M.; Fortun, D.; Borgers, S.; Heine, J.; Schloetel, J. G.; Reuss, M.; Unser, M.; Boyden, E. S.; Sauer, M.; Hamel, V.; Guichard, P. Imaging Cellular Ultrastructures Using Expansion Microscopy (U-ExM). *Nat. Methods* **2019**, *16* (1), 71−74.

(21) Laporte, M. H.; Klena, N.; Hamel, V.; Guichard, P. Visualizing the Native Cellular Organization by Coupling Cryofixation with Expansion Microscopy (Cryo-ExM). *Nat. Methods* **2022**, *19* (2), 216−222.

(22) Chen, F.; Wassie, A. T.; Cote, A. J.; Sinha, A.; Alon, S.; Asano, S.; Daugharthy, E. R.; Chang, J. B.; Marblestone, A.; Church, G. M.; Raj, A.; Boyden, E. S. Nanoscale Imaging of RNA with Expansion Microscopy. *Nat. Methods* **2016**, *13* (8), 679−684.

(23) Tillberg, P. W.; Chen, F.; Piatkevich, K. D.; Zhao, Y.; Yu, C. C.; English, B. P.; Gao, L.; Martorell, A.; Suk, H. J.; Yoshida, F.; Degennaro, E. M.; Roossien, D. H.; Gong, G.; Seneviratne, U.; Tannenbaum, S. R.; Desimone, R.; Cai, D.; Boyden, E. S. Protein-Retention Expansion Microscopy of Cells and Tissues Labeled Using Standard Fluorescent Proteins and Antibodies. *Nat. Biotechnol.* **2016**, *34* (9), 987−992.

(24) Chozinski, T. J.; Halpern, A. R.; Okawa, H.; Kim, H. J.; Tremel, G. J.; Wong, R. O. L.; Vaughan, J. C. Expansion Microscopy with Conventional Antibodies and Fluorescent Proteins. *Nat. Methods* **2016**, *13* (6), 485−488.

(25) Park, H.-E.; Choi, D.; Park, Su.; Sim, J.; Park, C.; Kang, S.; Yim, S.; Lee, H.; Kim, M.; Pac, J.; Rhee, J.; Lee, K.; Lee, J.; Lee, Y.; Kim, Y.; Park, S.-Y.; Park, H.; Sim, J. S.; Yim, C.; Lee, H.; Lee, M.; Kim, J.; Kim, S.; Rhee, J.; Choi, K.; Park, D.; Kang, S.; Pac, S.; Lee, J.; Lee, Y. Y. J. Scalable and Isotropic Expansion of Tissues with Simply Tunable Expansion Ratio. *Adv. Sci.* **2019**, *6* (22), No. 1901673.

(26) Damstra, H. G. J.; Mohar, B.; Eddison, M.; Akhmanova, A.; Kapitein, L. C.; Tillberg, P. W. Visualizing Cellular and Tissue Ultrastructure Using Ten-Fold Robust Expansion Microscopy (TREx). *ELife* **2022**, *11*, e73775.

(27) Mao, C.; Lee, M. Y.; Jhan, J. R.; Halpern, A. R.; Woodworth, M. A.; Glaser, A. K.; Chozinski, T. J.; Shin, L.; Pippin, J. W.; Shankland, S. J.; Liu, J. T. C.; Vaughan, J. C. Feature-Rich Covalent Stains for Super-Resolution and Cleared Tissue Fluorescence Microscopy. *Sci. Adv.* **2020**, *6* (22), 4542−4569.

(28) Karagiannis, E. D.; Kang, J. S.; Shin, T. W.; et al. IMAXT Grand Challenge Consortium, Marblestone, A.H., Kasthuri, N. and Boyden, E.S., 2019. Expansion Microscopy of Lipid Membranes. *bioRxiv* **2019**, No. 829903. (accessed November 07, 2019)

(29) Truckenbrodt, S.; Maidorn, M.; Crzan, D.; Wildhagen, H.; Kabatas, S.; Rizzoli, S. O. X10 Expansion Microscopy Enables 25-nm Resolution on Conventional Microscopes. *EMBO Rep.* **2018**, *19* (9), 45836.

(30) Sun, D. en.; Fan, X.; Shi, Y.; Zhang, H.; Huang, Z.; Cheng, B.; Tang, Q.; Li, W.; Zhu, Y.; Bai, J.; Liu, W.; Li, Y.; Wang, X.; Lei, X.;

Chen, X. Click-ExM Enables Expansion Microscopy for All Biomolecules. *Nat. Methods* **2021**, *18* (1), 107−113.

(31) Shi, X.; Li, Q.; Dai, Z.; Tran, A. A.; Feng, S.; Ramirez, A. D.; Lin, Z.; Wang, X.; Chow, T. T.; Chen, J.; Kumar, D.; McColloch, A. R.; Reiter, J. F.; Huang, E. J.; Seiple, I. B.; Huang, B. Label-Retention Expansion Microscopy. *J. Cell Biol.* **2021**, *220* (9), e202105067.

(32) Gao, R.; Asano, S. M.; Upadhyayula, S.; Pisarev, I.; Milkie, D. E.; Liu, T. L.; Singh, V.; Graves, A.; Huynh, G. H.; Zhao, Y.; Bogovic, J.; Colonell, J.; Ott, C. M.; Zugates, C.; Tappan, S.; Rodriguez, A.; Mosaliganti, K. R.; Sheu, S. H.; Pasolli, H. A.; Pang, S.; Xu, C. S.; Megason, S. G.; Hess, H.; Lippincott-Schwartz, J.; Hantman, A.; Rubin, G. M.; Kirchhausen, T.; Saalfeld, S.; Aso, Y.; Boyden, E. S.; Betzig, E. Cortical Column and Whole-Brain Imaging with Molecular Contrast and Nanoscale Resolution. *Science* **2019**, *363* (6424), eaau8302.

(33) Chozinski, T. J.; Mao, C.; Halpern, A. R.; Pippin, J. W.; Shankland, S. J.; Alpers, C. E.; Najafian, B.; Vaughan, J. C. Volumetric, Nanoscale Optical Imaging of Mouse and Human Kidney via Expansion Microscopy. *Sci. Rep.* **2018**, *8* (1), 10396.

(34) Park, C. E.; Cho, Y.; Cho, I.; Jung, H.; Kim, B.; Shin, J. H.; Choi, S.; Kwon, S. K.; Hahn, Y. K.; Chang, J. B. Super-Resolution Three-Dimensional Imaging of Actin Filaments in Cultured Cells and the Brain via Expansion Microscopy. *ACS Nano* **2020**, *14* (11), 14999−15010.

(35) Chang, J. B.; Chen, F.; Yoon, Y. G.; Jung, E. E.; Babcock, H.; Kang, J. S.; Asano, S.; Suk, H. J.; Pak, N.; Tillberg, P. W.; Wassie, A. T.; Cai, D.; Boyden, E. S. Iterative Expansion Microscopy. *Nat. Methods* **2017**, *14* (6), 593−599.

(36) Ku, T.; Swaney, J.; Park, J. Y.; Albanese, A.; Murray, E.; Cho, H.; Park, J.; Mangena, Y. G.; Chen, V.; Chung, J. K. Multiplexed and Scalable Super-Resolution Imaging of Three-Dimensional Protein Localization in Size-Adjustable Tissues. *Nat. Biotechnol.* **2016**, *34* (9), 973−981.

(37) Halpern, A. R.; Alas, G. C. M.; Chozinski, T. J.; Paredez, A. R.; Vaughan, J. C. Hybrid Structured Illumination Expansion Microscopy Reveals Microbial Cytoskeleton Organization. *ACS Nano* **2017**, *11* (12), 12677−12686.

(38) Jiang, N.; Kim, H. J.; Chozinski, T. J.; Azpurua, J. E.; Eaton, B. A.; Vaughan, J. C.; Parrish, J. Z. Superresolution Imaging of Drosophila Tissues Using Expansion Microscopy. *Mol. Biol. Cell* **2018**, *29* (12), 1413−1421.

(39) Freifeld, L.; Odstrcil, I.; Förster, D.; Ramirez, A.; Gagnon, J. A.; Randlett, O.; Costa, E. K.; Asano, S.; Celiker, O. T.; Gao, R.; Martin-Alarcon, D. A.; Reginato, P.; Dick, C.; Chen, L.; Schoppik, D.; Engert, F.; Baier, H.; Boyden, E. S. Expansion Microscopy of Zebrafish for Neuroscience and Developmental Biology Studies. *Proc. Natl. Acad. Sci. U.S.A.* **2017**, *114* (50), E10799−E10808.

(40) Bertiaux, E.; Balestra, A. C.; Bournonville, L.; Louvel, V.; Maco, B.; Soldati-Favre, D.; Brochet, M.; Guichard, P.; Hamel, V. Expansion Microscopy Provides New Insights into the Cytoskeleton of Malaria Parasites Including the Conservation of a Conoid. *PLoS Biol.* **2021**, *19* (3), No. e3001020.

(41) Yu, C. C.; Barry, N. C.; Wassie, A. T.; Sinha, A.; Bhattacharya, A.; Asano, S.; Zhang, C.; Chen, F.; Hobert, O.; Goodman, M. B.; Haspel, G.; Boyden, E. S. Expansion Microscopy of *C. Elegans*. *eLife* **2020**, *9*, e46249.

(42) Steib, E.; Tetley, R.; Laine, R. F.; Norris, D. P.; Mao, Y.; Vermot, J. TissUExM Enables Quantitative Ultrastructural Analysis in Whole Vertebrate Embryos by Expansion Microscopy. *Cell Rep. Methods* **2022**, *2* (10), No. 100311.

(43) Mu, J.; Slevin, J. C.; Qu, D.; McCormick, S.; Adamson, S. L. In Vivo Quantification of Embryonic and Placental Growth during Gestation in Mice Using Micro-Ultrasound. *Reprod. Biol. Endocrinol.* **2008**, *6*, 34.

(44) Wang, Q.; Du, L.; Wang, Y.; Xu, C.; Sun, Z.; Fu, Y.; Yang, B.; Wang, Y.; Mu, C.; Fan, S.; Cai, L.; Katsube, T.; Liu, Q. The Development and Biological Characteristics of a Novel Potentially Radioresistant Inbred Mouse Strain. *Mol. Med. Rep.* **2017**, *15* (2), 759−767.

(45) Czerwinska, A. M.; Grabowska, I.; Archacka, K.; Bem, J.; Swierczek, B.; Helinska, A.; Streminska, W.; Fogtman, A.; Iwanicka-Nowicka, R.; Koblowska, M.; Ciemerych, M. A. Myogenic Differentiation of Mouse Embryonic Stem Cells That Lack a Functional Pax7 Gene. *Stem Cells Dev.* **2016**, *25* (4), 285.

(46) Oest, M. E.; Jones, J. C.; Hatfield, C.; Prater, M. R. Micro-CT Evaluation of Murine Fetal Skeletal Development Yields Greater Morphometric Precision over Traditional Clear-Staining Methods. *Birth Defects Res., Part B* **2008**, *83* (6), 582−589.

(47) Handschuh, S.; Glösmann, M. Mouse Embryo Phenotyping Using X-Ray MicroCT. *Front. Cell Dev. Biol.* **2022**, *10*, 949184.

(48) Gabner, S.; Böck, P.; Fink, D.; Glösmann, M.; Handschuh, S. The Visible Skeleton 2.0: Phenotyping of Cartilage and Bone in Fixed Vertebrate Embryos and Foetuses Based on X-Ray MicroCT. *Development* **2020**, *147* (11), dev187633.

(49) Sheard, T. M. D.; Shakespeare, T. B.; Seehra, R. S.; Spencer, M. E.; Suen, K. M.; Jayasinghe, I. Differential Labelling of Human Sub-Cellular Compartments with Fluorescent Dye Esters and Expansion Microscopy. *Nanoscale* **2023**, *15* (45), 18489−18499.

(50) Krauss, R. S.; Chihara, D.; Romer, A. I. Embracing Change: Striated-for-Smooth Muscle Replacement in Esophagus Development. *Skeletal Muscle* **2016**, *6* (1), 27.

(51) Merrell, A. J.; Kardon, G. Development of the Diaphragm − a Skeletal Muscle Essential for Mammalian Respiration. *FEBS J.* **2013**, *280* (17), 4026−4035.

(52) Nassari, S.; Duprez, D.; Fournier-Thibault, C. Non-Myogenic Contribution to Muscle Development and Homeostasis: The Role of Connective Tissues. *Front. Cell Dev. Biol.* **2017**, *5*, No. 249992.

(53) Connective Tissues *Cell Biol.* 2017, pp 555−570 .

(54) Kamrani, P.; Marston, G.; Arbor, T. C.; Jan, A. Connective Tissue *StatPearls* 2024.

(55) Di Lullo, G. A.; Sweeney, S. M.; Körkkö, J.; Ala-Kokko, L.; San Antonio, J. D. Mapping the Ligand-Binding Sites and Disease-Associated Mutations on the Most Abundant Protein in the Human, Type I Collagen. *J. Biol. Chem.* **2002**, *277* (6), 4223−4231.

(56) Ma, R.; Štefl, M.; Nienhaus, G. U. Single Molecule Localization-Based Analysis of Clathrin-Coated Pit and Caveolar Dynamics. *Nanoscale Horizons* **2022**, *7* (4), 385−395.

(57) Heuser, J.; Evans, L. Three-Dimensional Visualization of Coated Vesicle Formation in Fibroblasts. *J. Cell Biol.* **1980**, *84* (3), 560−583.

(58) Khotimah; Yuliyani, H.; Nuraenah, E.; Zahara, E.; Khotimah, H.; Kalsum, U.; Nurdiana; Ali, M. M. Centella Asiatica Increased the Body Length through the Modulation of Antioxidant in Rotenone-Induced Zebrafish Larvae. *Biomed. Pharmacol. J.* **2018**, *11* (2), 827−833.

(59) Choi, J.; Dong, L.; Ahn, J.; Dao, D.; Hammerschmidt, M.; Chen, J. N. FoxH1 Negatively Modulates Flk1 Gene Expression and Vascular Formation in Zebrafish. *Dev. Biol.* **2007**, *304* (2), 735−744.

(60) Huang, C. J.; Tu, C. T.; Hsiao, C. D.; Hsieh, F. J.; Tsai, H. J. Germ-Line Transmission of a Myocardium-Specific GFP Transgene Reveals Critical Regulatory Elements in the Cardiac Myosin Light Chain 2 Promoter of Zebrafish. *Dev. Dyn.* **2003**, *228* (1), 30−40.

(61) Jung, S.; Kuo, W. P.; Nimmagadda, S.; Benson, S. L.; Geetha-Loganathan, P.; Logan, C.; Au-Yeung, T.; Chiang, E.; Fu, K.; Richman, J. M. Visualization of Myelination in GFP-Transgenic Zebrafish. *Dev. Dyn.* **2010**, *239* (2), 592−597.

(62) Kidoya, H.; Ueno, M.; Yamada, Y.; Mochizuki, N.; Nakata, M.; Yano, T.; Fujii, R.; Takakura, N. Spatial and Temporal Role of the Apelin/APJ System in the Caliber Size Regulation of Blood Vessels during Angiogenesis. *EMBO J.* **2008**, *27* (3), 522−534.

(63) Yarilin, D.; Xu, K.; Turkekul, M.; Fan, N.; Romin, Y.; Fijisawa, S.; Barlas, A.; Manova-Todorova, K. Machine-Based Method for Multiplex in Situ Molecular Characterization of Tissues by Immunofluorescence Detection. *Sci. Rep.* **2015**, *5*, 9534.

(64) Yokomizo, T.; Yamada-Inagawa, T.; Yzaguirre, A. D.; Chen, M. J.; Speck, N. A.; Dzierzak, E. Whole-Mount Three-Dimensional Imaging of Internally Localized Immunostained Cells within Mouse Embryos. *Nat. Protoc.* **2012**, *7* (3), 421−431.

(65) Bajanca, F.; Luz, M.; Raymond, K.; Martins, G. G.; Sonnenberg, A.; Tajbakhsh, S.; Buckingham, M. Thorsteinsdóttir, S. Integrin A6β1-Laminin Interactions Regulate Early Myotome Formation in the Mouse Embryo. *Development* **2006**, *133* (9), 1635−1644.

(66) Li, Q.; Zhang, Z.; Li, Z.; Zhou, M.; Liu, B.; Pan, L.; Ma, Z.; Zheng, Y. ADAM17 Is Critical for Multipolar Exit and Radial Migration of Neuronal Intermediate Progenitor Cells in Mice Cerebral Cortex. *PLoS One* **2013**, *8* (6), No. e65703.

(67) Lee, S. K.; Jurata, L. W.; Funahashi, J.; Ruiz, E. C.; Pfaff, S. L. Analysis of Embryonic Motoneuron Gene Regulation: Derepression of General Activators Function in Concert with Enhancer Factors. *Development* **2004**, *131* (14), 3295−3306.

(68) Saal, K. A.; Shaib, A. H.; Mougios, N.; Crzan, D.; Opazo, F.; Rizzoli, S. O. Heat Denaturation Enables Multicolor X10-STED Microscopy. *Sci. Rep.* **2023**, *13* (1), 5366.

(69) Wolfson, R. L.; Abdelaziz, A.; Rankin, G.; Kushner, S.; Qi, L.; Mazor, O.; Choi, S.; Sharma, N.; Ginty, D. D. DRG Afferents That Mediate Physiologic and Pathologic Mechanosensation from the Distal Colon. *Cell* **2023**, *186* (16), 3368−3385.

(70) Kim, A. Y.; Tang, Z.; Liu, Q.; Patel, K. N.; Maag, D.; Geng, Y.; Dong, X. Pirt, a Phosphoinositide-Binding Protein, Functions as a Regulatory Subunit of TRPV1. *Cell* **2008**, *133* (3), 475.

(71) Breit, S.; Kupferberg, A.; Rogler, G.; Hasler, G. Vagus Nerve as Modulator of the Brain-Gut Axis in Psychiatric and Inflammatory Disorders. *Front. Psychiatry* **2018**, *9*, No. 44.

(72) Carotenuto, A.; Wilson, H.; Giordano, B.; Caminiti, S. P.; Chappell, Z.; Williams, S. C. R.; Hammers, A.; Silber, E.; Brex, P.; Politis, M. Impaired Connectivity within Neuromodulatory Networks in Multiple Sclerosis and Clinical Implications. *J. Neurol.* **2020**, *267* (7), 2042−2053.

(73) Rubio, M. A.; Herrando-Grabulosa, M.; Navarro, X. Sensory Involvement in Amyotrophic Lateral Sclerosis. *Int. J. Mol. Sci.* **2022**, *23* (24), 15521.

(74) McCray, B. A.; Scherer, S. S. Axonal Charcot-Marie-Tooth Disease: From Common Pathogenic Mechanisms to Emerging Treatment Opportunities. *Neurotherapeutics* **2021**, *18* (4), 2269−2285.

(75) Uesaka, T.; Okamoto, M.; Nagashimada, M.; Tsuda, Y.; Kihara, M.; Kiyonari, H.; Enomoto, H. Enhanced Enteric Neurogenesis by Schwann Cell Precursors in Mouse Models of Hirschsprung Disease. *Glia* **2021**, *69* (11), 2575−2590.

(76) Ha, J. L. H.; Lui, V. C. H.; Tam, P. K. H. Embryology and Anatomy of Hirschsprung Disease. *Semin. Pediatr. Surg.* **2022**, *31* (6), No. 151227.

(77) Chen, D.; Xie, R.; Shu, B.; Landay, A. L.; Wei, C.; Reiser, J.; Spagnoli, A.; Torquati, A.; Forsyth, C. B.; Keshavarzian, A.; Sumner, D. R. Wnt Signaling in Bone, Kidney, Intestine, and Adipose Tissue and Interorgan Interaction in Aging. *Ann. N.Y. Acad. Sci.* **2019**, *1442* (1), 48−60.

(78) Huh, J. R.; Veiga-Fernandes, H. Neuroimmune Circuits in Inter-Organ Communication. *Nat. Rev. Immunol.* **2020**, *20* (4), 217−228.

(79) Bischoff, J. P.; Schulz, A.; Morrison, H. The Role of Exosomes in Intercellular and Inter-Organ Communication of the Peripheral Nervous System. *FEBS Lett.* **2022**, *596* (5), 655−664.

(80) Goldberger, J. J.; Arora, R.; Buckley, U.; Shivkumar, K. Autonomic Nervous System Dysfunction: JACC Focus Seminar. *J. Am. Coll. Cardiol.* **2019**, *73* (10), 1189−1206.

(81) Shi, X.; Li, Q.; Dai, Z.; Tran, A. A.; Feng, S.; Ramirez, A. D.; Lin, Z.; Wang, X.; Chow, T. T.; Chen, J.; Kumar, D.; McColloch, A. R.; Reiter, J. F.; Huang, E. J.; Seiple, I. B.; Huang, B. Label-Retention Expansion Microscopy. *J. Cell Biol.* **2021**, *220* (9), e202105067.

(82) Thomasen, P. B.; Salasova, A.; Kjaer-Sorensen, K.; Woloszczuková, L.; Lavický, J.; Login, H.; Tranberg-Jensen, J.; Almeida, S.; Beel, S.; Kavková, M.; Qvist, P.; Kjolby, M.; Ovesen, P. L.; Nolte, S.; Vestergaard, B.; Udrea, A. C.; Nejsum, L. N.; Chao, M. V.; Van Damme, P.; Krivanek, J.; Dasen, J.; Oxvig, C.; Nykjaer, A. SorCS2 Binds Progranulin to Regulate Motor Neuron Development. *Cell Rep.* **2023**, *42* (11), 113333.

(83) Chandrasekhar, A. Turning Heads: Development of Vertebrate Branchiomotor Neurons. *Dev. Dyn.* **2004**, *229* (1), 143−161.

(84) Asakawa, K.; Kawakami, K. Protocadherin-Mediated Cell Repulsion Controls the Central Topography and Efferent Projections of the Abducens Nucleus. *Cell Rep.* **2018**, *24* (6), 1562−1572.

(85) Huettl, R. E.; Huber, A. B. Cranial Nerve Fasciculation and Schwann Cell Migration Are Impaired after Loss of Npn-1. *Dev. Biol.* **2011**, *359* (2), 230−241.

(86) Huettl, R. E.; Eckstein, S.; Stahl, T.; Petricca, S.; Ninkovic, J.; Götz, M.; Huber, A. B. Functional Dissection of the Pax6 Paired Domain: Roles in Neural Tube Patterning and Peripheral Nervous System Development. *Dev. Biol.* **2016**, *413* (1), 86−103.

(87) Park, J. G.; Tischfield, M. A.; Nugent, A. A.; Cheng, L.; Di Gioia, S. A.; Chan, W. M.; Maconachie, G.; Bosley, T. M.; Summers, C. G.; Hunter, D. G.; Robson, C. D.; Gottlob, I.; Engle, E. C. Loss of MAFB Function in Humans and Mice Causes Duane Syndrome, Aberrant Extraocular Muscle Innervation, and Inner-Ear Defects. *Am. J. Hum. Genet.* **2016**, *98* (6), 1220−1227.

(88) Kim, S. W.; Kim, K. T. Expression of Genes Involved in Axon Guidance: How Much Have We Learned? *Int. J. Mol. Sci.* **2020**, *21* (10), 3566.

(89) Lesnick, T. G.; Papapetropoulos, S.; Mash, D. C.; Ffrench-Mullen, J.; Shehadeh, L.; De Andrade, M.; Henley, J. R.; Rocca, W. A.; Ahlskog, J. E.; Maraganore, D. M. A Genomic Pathway Approach to a Complex Disease: Axon Guidance and Parkinson Disease. *PLoS Genetics* **2007**, *3* (6), No. e98.

(90) Steyer, A. M.; Ruhwedel, T.; Nardis, C.; Werner, H. B.; Nave, K. A.; Möbius, W. Pathology of Myelinated Axons in the PLP-Deficient Mouse Model of Spastic Paraplegia Type 2 Revealed by Volume Imaging Using Focused Ion Beam-Scanning Electron Microscopy. *J. Struct. Biol.* **2020**, *210* (2), No. 107492.

(91) Hibbitts, A. J.; Kočí, Z.; Kneafsey, S.; Matsiko, A.; Žilić, L.; Dervan, A.; Hinton, P.; Chen, G.; Cavanagh, B.; Dowling, J. K.; McCoy, C. E.; Buckley, C. T.; Archibald, S. J.; O'Brien, F. J. Multi-Factorial Nerve Guidance Conduit Engineering Improves Outcomes in Inflammation, Angiogenesis and Large Defect Nerve Repair. *Matrix Biol.* **2022**, *106*, 34−57.

(92) Rha, A. K.; Maguire, A. S.; Martin, D. R. GM1 Gangliosidosis: Mechanisms and Management. *Appl. Clin. Genetics* **2021**, *14*, 209−233.

(93) Schechter, M.; Grigoletto, J.; Abd-Elhadi, S.; Glickstein, H.; Friedman, A.; Serrano, G. E.; Beach, T. G.; Sharon, R. A Role for α-Synuclein in Axon Growth and Its Implications in Corticostriatal Glutamatergic Plasticity in Parkinson's Disease. *Mol. Neurodegener.* **2020**, *15* (1), 24.

(94) Lee, J. Y.; Kim, M. J.; Li, L.; Velumian, A. A.; Aui, P. M.; Fehlings, M. G.; Petratos, S. Nogo Receptor 1 Regulates Caspr Distribution at Axo-Glial Units in the Central Nervous System. *Sci. Rep.* **2017**, *7* (1), 8958.

(95) Chen, Y. F.; Chen, L. H.; Yeh, Y. M.; Wu, P. Y.; Chen, Y. F.; Chang, L. Y.; Chang, J. Y.; Shen, M. R. Minoxidil Is a Potential Neuroprotective Drug for Paclitaxel-Induced Peripheral Neuropathy. *Sci. Rep.* **2017**, *7*, 45366.

(96) Min, K.; Cho, I.; Choi, M.; Chang, J. B. Multiplexed Expansion Microscopy of the Brain through Fluorophore Screening. *Methods* **2020**, *174*, 3−10.

(97) Tomer, R.; Ye, L.; Hsueh, B.; Deisseroth, K. Advanced CLARITY for Rapid and High-Resolution Imaging of Intact Tissues. *Nat. Protocols* **2014**, *9* (7), 1682−1697.

(98) Miwatani-Minter, B.; Rona, G. Laser Micro-Irradiation to Study DNA Recruitment During S Phase. *J. Vis. Exp.* **2021**, *2021* (170), e62466.

(99) Chhetri, R. K.; Amat, F.; Wan, Y.; Höckendorf, B.; Lemon, W. C.; Keller, P. J. Whole-Animal Functional and Developmental Imaging with Isotropic Spatial Resolution. *Nat. Methods* **2015**, *12* (12), 1171−1178.

(100) Young, P.; Qiu, L.; Wang, D.; Zhao, S.; Gross, J.; Feng, G. Single-Neuron Labeling with Inducible Cre-Mediated Knockout in Transgenic Mice. *Nat. Neurosci.* **2008**, *11* (6), 721−728.

(101) Matho, K. S.; Huilgol, D.; Galbavy, W.; He, M.; Kim, G.; An, X.; Lu, J.; Wu, P.; Di Bella, D. J.; Shetty, A. S.; Palaniswamy, R.; Hatfield, J.; Raudales, R.; Narasimhan, A.; Gamache, E.; Levine, J. M.; Tucciarone, J.; Szelenyi, E.; Harris, J. A.; Mitra, P. P.; Osten, P.; Arlotta, P.; Huang, Z. J. Genetic Dissection of the Glutamatergic Neuron System in Cerebral Cortex. *Nature* **2021**, *598* (7879), 182−187.

(102) Snippert, H. J.; van der Flier, L. G.; Sato, T.; van Es, J. H.; van den Born, M.; Kroon-Veenboer, C.; Barker, N.; Klein, A. M.; van Rheenen, J.; Simons, B. D.; Clevers, H. Intestinal Crypt Homeostasis Results from Neutral Competition between Symmetrically Dividing Lgr5 Stem Cells. *Cell* **2010**, *143* (1), 134−144.

(103) Boone, P. G.; Rochelle, L. K.; Ginzel, J. D.; Lubkov, V.; Roberts, W. L.; Nicholls, P. J.; Bock, C.; Flowers, M. L.; von Furstenberg, R. J.; Stripp, B. R.; Agarwal, P.; Borowsky, A. D.; Cardiff, R. D.; Barak, L. S.; Caron, M. G.; Lyerly, H. K.; Snyder, J. C. A Cancer Rainbow Mouse for Visualizing the Functional Genomics of Oncogenic Clonal Expansion. *Nat. Commun.* **2019**, *10* (1), 5490.

(104) Sereti, K. I.; Nguyen, N. B.; Kamran, P.; Zhao, P.; Ranjbarvaziri, S.; Park, S.; Sabri, S.; Engel, J. L.; Sung, K.; Kulkarni, R. P.; Ding, Y.; Hsiai, T. K.; Plath, K.; Ernst, J.; Sahoo, D.; Mikkola, H. K. A.; Iruela-Arispe, M. L.; Ardehali, R. Analysis of Cardiomyocyte Clonal Expansion during Mouse Heart Development and Injury. *Nat. Commun.* **2018**, *9* (1), 754.

(105) Tabansky, I.; Lenarcic, A.; Draft, R. W.; Loulier, K.; Keskin, D. B.; Rosains, J.; Rivera-Feliciano, J.; Lichtman, J. W.; Livet, J.; Stern, J. N. H.; Sanes, J. R.; Eggan, K. Developmental Bias in Cleavage-Stage Mouse Blastomeres. *Curr. Biol.* **2013**, *23* (1), 21−31.

(106) M'Saad, O.; Bewersdorf, J. All-Optical Visualization of Specific Molecules in the Ultrastructural Context of Brain Tissue. US18/295,446.2023.

(107) Renier, N.; Adams, E. L.; Kirst, C.; Wu, Z.; Azevedo, R.; Kohl, J.; Autry, A. E.; Kadiri, L.; Umadevi Venkataraju, K.; Zhou, Y.; Wang, V. X.; Tang, C. Y.; Olsen, O.; Dulac, C.; Osten, P.; Tessier-Lavigne, M. Mapping of Brain Activity by Automated Volume Analysis of Immediate Early Genes. *Cell* **2016**, *165* (7), 1789−1802.

(108) Zhao, S.; Todorov, M. I.; Cai, R.; Maskari, R. A.; Steinke, H.; Kemter, E.; Mai, H.; Rong, Z.; Warmer, M.; Stanic, K.; Schoppe, O.; Paetzold, J. C.; Gesierich, B.; Wong, M. N.; Huber, T. B.; Duering, M.; Bruns, O. T.; Menze, B.; Lipfert, J.; Puelles, V. G.; Wolf, E.; Bechmann, I.; Ertürk, A. Cellular and Molecular Probing of Intact Human Organs. *Cell* **2020**, *180* (4), 796−812.

(109) Mai, H.; Luo, J.; Hoeher, L.; Al-Maskari, R.; Horvath, I.; Chen, Y.; Kofler, F.; Piraud, M.; Paetzold, J. C.; Modamio, J.; Todorov, M.; Elsner, M.; Hellal, F.; Ertürk, A. Whole-Body Cellular Mapping in Mouse Using Standard IgG Antibodies. *Nat. Biotechnol.* **2023**, *42* (4), 617−627.

(110) Murray, E.; Cho, J. H.; Goodwin, D.; Ku, T.; Swaney, J.; Kim, S. Y.; Choi, H.; Park, Y. G.; Park, J. Y.; Hubbert, A.; McCue, M.; Vassallo, S.; Bakh, N.; Frosch, M. P.; Wedeen, V. J.; Seung, H. S.; Chung, K. Simple, Scalable Proteomic Imaging for High-Dimensional Profiling of Intact Systems. *Cell* **2015**, *163* (6), 1500−1514.

(111) Park, Y. G.; Sohn, C. H.; Chen, R.; McCue, M.; Yun, D. H.; Drummond, G. T.; Ku, T.; Evans, N. B.; Oak, H. C.; Trieu, W.; Choi, H.; Jin, X.; Lilascharoen, V.; Wang, J.; Truttmann, M. C.; Qi, H. W.; Ploegh, H. L.; Golub, T. R.; Chen, S. C.; Frosch, M. P.; Kulik, H. J.; Lim, B. K.; Chung, K. Protection of Tissue Physicochemical Properties Using Polyfunctional Crosslinkers. *Nat. Biotechnol.* **2019**, *37* (1), 73−83.

(112) Yun, D. H.; Park, Y.-G.; Cho, J. H. etc. Ultrafast Immunostaining of Organ-Scale Tissues for Scalable Proteomic Phenotyping *bioRxiv*. 2019; Vol. *660373* DOI: 10.1101/660373. (accessed June 10, 2019).

(113) Cho, Y.; Seo, J.; Sim, Y.; Chung, J.; Park, C. E.; Park, C. G.; Kim, D.; Chang, J. B. FRACTAL: Signal Amplification of Immunofluorescence via Cyclic Staining of Target Molecules. *Nanoscale* **2020**, *12* (46), 23506−23513.

(114) Min, K.; Cho, I.; Choi, M.; Chang, J. B. Multiplexed Expansion Microscopy of the Brain through Fluorophore Screening. *Methods* **2020**, *174*, 3−10.

(115) Klimas, A.; Gallagher, B. R.; Wijesekara, P.; Fekir, S.; DiBernardo, E. F.; Cheng, Z.; Stolz, D. B.; Cambi, F.; Watkins, S. C.; Brody, S. L.; Horani, A.; Barth, A. L.; Moore, C. I.; Ren, X.; Zhao, Y. Magnify Is a Universal Molecular Anchoring Strategy for Expansion Microscopy. *Nat. Biotechnol.* **2023**, *41* (6), 858−869.

(116) Gao, R.; Yu, C. C.; Gao, L.; Piatkevich, K. D.; Neve, R. L.; Munro, J. B.; Upadhyayula, S.; Boyden, E. S. A Highly Homogeneous Polymer Composed of Tetrahedron-like Monomers for High-Isotropy Expansion Microscopy. *Nat. Nanotechnol.* **2021**, *16* (6), 698−707.

(117) Peng, T.; Thorn, K.; Schroeder, T.; Wang, L.; Theis, F. J.; Marr, C.; Navab, N. A BaSiC Tool for Background and Shading Correction of Optical Microscopy Images. *Nat. Commun.* **2017**, *8* (1), 14836.

(118) Eom, M.; Han, S.; Park, P.; Kim, G.; Cho, E. S.; Sim, J.; Lee, K. H.; Kim, S.; Tian, H.; Böhm, U. L.; Lowet, E.; Tseng, H. an.; Choi, J.; Lucia, S. E.; Ryu, S. H.; Rózsa, M.; Chang, S.; Kim, P.; Han, X.; Piatkevich, K. D.; Choi, M.; Kim, C. H.; Cohen, A. E.; Chang, J. B.; Yoon, Y. G. Statistically Unbiased Prediction Enables Accurate Denoising of Voltage Imaging Data. *Nat. Methods* **2023**, *20* (10), 1581−1592.